

An unbiased computational contact formulation for 3D friction

Roger A. Sauer ^{1,a} and Laura De Lorenzis^b

^aGraduate School AICES, RWTH Aachen University, Templergraben 55, 52056 Aachen, Germany;
sauer@aices.rwth-aachen.de

^bInstitute of Applied Mechanics, TU Braunschweig, Bienroder Weg 87, 38106 Braunschweig,
Germany, l.delorenzis@tu-braunschweig.de

Published² in *International Journal of Numerical Methods in Engineering*, DOI: [10.1002/nme.4794](https://doi.org/10.1002/nme.4794)
Submitted on 27. February 2013, Revised on 13. June 2014, Accepted on 14. August 2014

Abstract:

A new computational contact formulation is presented and analyzed for large deformation frictional contact. The new formulation uses an unbiased treatment of the two neighboring contact surfaces considering the two-half-pass contact algorithm, originally derived for frictionless contact. The presented work thus introduces several novelties to unbiased friction algorithms. The new algorithm does not enforce traction continuity at the contact interface explicitly, but rather satisfies it intrinsically to high accuracy, as is shown. A new 3D friction formulation is also proposed that is a direct extension of the 1D setup, expressing the friction variables in the parameter space used for the curvilinear surface description. The new formulation resorts to classical expressions in the continuum limit. The current approach uses C^1 -smooth contact surface representations based on either Hermite or NURBS interpolation. A penalty regularization is considered for the impenetrability and tangential sticking constraints. The new, unbiased friction formulation is illustrated by several 2D and 3D examples, which include an extensive analysis of the model parameters, a convergence study and the comparison with a classical biased master/slave contact algorithm.

Keywords: computational contact mechanics, isogeometric analysis, non-linear continuum mechanics, predictor-corrector algorithm, sticking and sliding friction, two-pass algorithms

1 Introduction

This work is concerned with unbiased contact formulations, which treat both contact surfaces equally. This treatment is in contrast to most contact formulations, which introduce a bias by treating the surfaces differently, usually in the context of a master/slave or mortar/non-mortar designation. In an earlier paper, we have presented a new contact formulation that appears naturally if contact is derived from pairwise surface potentials [1]. The formulation is motivated from general surface interactions, like adhesion and electrostatics. Apart from those, the potential formulation also admits classical contact formulations, like penalty and barrier methods. The new formulation leads to an unbiased two-pass contact algorithm, where each pass accounts only for half of the contributions of common one-pass approaches, and it was therefore termed *two-half-pass contact algorithm*. It turned out that in the case of the penalty method, the resulting formulation of [1] is very similar to the earlier work of Papadopoulos and co-workers [2]. The only differences between [1] and [2] lie in the definition of the gap function

¹Corresponding author, email: sauer@aices.rwth-aachen.de

²This pdf is the personal version of an article whose final publication is available at [wileyonlinelibrary.com](https://www.wileyonlinelibrary.com)

and in the constraint enforcement, which in our case is considered at the quadrature level like in [3] and [4].

In subsequent work by Papadopoulos and co-workers, [2] is extended to Lagrange multipliers considering 2D [5] and 3D [6] contact implementations. There, the authors include a continuity enforcement of the contact traction into the numerical formulation and consider a patterning of the surface nodes, distinguishing between nodes where the gap is constrained and nodes where pressure continuity is enforced. This setup is then later used to develop 2D and 3D friction formulations that are unbiased [7; 8]. This is different from our approach. Here, the contact traction continuity is not enforced explicitly. Instead it is obtained naturally to high accuracy in computations, since traction continuity is satisfied in the continuum limit of the formulation, as is proven in [1] for the frictionless case. For the numerical examples investigated so far, the continuity error is of the same order than the discretization error. Further, in our case, the contact constraints (impenetrability and sticking) are not enforced exactly, but only approximately up to the accuracy of mesh discretization.

The approach taken here also considers a new 3D friction formulation for large deformations, which tries to remedy some of the inconsistencies present in previous formulations. The new formulation becomes equal to the friction formulation of [9] and [10] in the continuum limit, as the temporal discretization approaches zero. In order to circumvent some of the pathologies resulting from sliding on discrete surfaces, we use C^1 -smooth surface representations based on Hermite (in 2D) and NURBS interpolations (in 3D). Such formulations have recently been developed for frictionless [11; 12; 13; 14] and frictional contact [15; 16; 17]. Here the surface interpolation is used directly within the interpolation of the deformation field, which distinguishes the formulations from surface smoothing methods that have been used in the past for friction, e.g. see [18; 19; 20]. The current work considers a penalty regularization of both contact constraints. The contact conditions are enforced at the quadrature level as in the formulations of [3] and [4]. The computational stability of this approach is discussed in Secs. 3 and 4.3.

To summarize, the new aspects of this work are:

- a new friction formulation for large-deformation contact that is similar but not identical to [9] and [10],
- a corresponding new frictional contact algorithm that is based on the concept of *two half-passes* going back to [2] and [1],
- contrary to prior work [7; 8], our friction algorithm does not enforce traction continuity, nor does it use nodal patterning for the contact constraints,
- the new algorithm thus uses separate traction fields and active sets on the two surfaces that are not directly coupled,
- the new algorithm is compared extensively with its – well established – full-pass counterpart considering several challenging 2D and 3D contact examples,
- it considers C^1 -smooth surface descriptions based on Hermite and NURBS interpolation, which have not been applied to a frictional two-half pass setting before, and in the case of Hermite not even applied to any frictional two-deformable-body contact setting before.

The remainder of this paper is organized as follows: Sec. 2 presents the friction formulation in the general 3D continuum mechanical framework of large deformations. Temporal discretization is considered, leading to the friction algorithm. Spatial discretization in the framework of the finite element method is then discussed in Sec. 3, both for the classical full-pass approach and the two-half-pass approach. Numerical examples are then presented in Sec. 4. The paper concludes with Sec. 5.

2 Friction formulations for large deformation contact

This section presents the 3D friction formulation that is considered in this work. The formulation is based on a classical predictor-corrector algorithm to advance friction locally through the states of sticking and sliding. The presented formulation is based on the treatment in 1D, which leads to some differences compared to existing friction formulations, as is shown.

2.1 Sticking and sliding

Given the contact surface, the contact traction \mathbf{t}_c can be decomposed into a normal and tangential part, written as

$$\mathbf{t}_c = \mathbf{t}_n + \mathbf{t}_t . \quad (1)$$

In [1] we have extensively discussed formulations for the normal contact traction \mathbf{t}_n . For frictional contact, the tangential traction \mathbf{t}_t is determined by the behavior during sticking and sliding. The distinction between these two states is based on a slip criterion of the form

$$f_s \begin{cases} < 0 & \text{sticking ,} \\ = 0 & \text{sliding .} \end{cases} \quad (2)$$

An example for the slip function f_s is

$$f_s = \|\mathbf{t}_t\| - \mu p \quad (3)$$

which corresponds to a cone in $\{p, \mathbf{t}_t\}$ -space. Here $p := \|\mathbf{t}_n\|$ denotes the contact pressure, while μ denotes the coefficient of friction.³ During sticking, the traction \mathbf{t}_t is defined by the constraint that no relative tangential motion occurs. During sliding, the traction \mathbf{t}_t is characterized by a sliding law, like Coulomb's law

$$\mathbf{t}_t = -\mu p \frac{\dot{\mathbf{g}}_t}{\|\dot{\mathbf{g}}_t\|} , \quad (4)$$

where $\dot{\mathbf{g}}_t$ denotes the relative tangential sliding velocity between the surfaces. The sticking constraint can be regularized by a penalty approach, which is considered here. This regularization allows for a small amount of tangential slip, denoted $\Delta \mathbf{g}_e$, that is reversible (thus 'elastic') upon unloading. Denoting the remaining, irreversible slip that is associated with sliding by \mathbf{g}_s , the total tangential slip \mathbf{g}_t thus decomposes into

$$\mathbf{g}_t = \mathbf{g}_s + \Delta \mathbf{g}_e . \quad (5)$$

Algorithmically, the state changes between sticking and slipping are usually based on a predictor-corrector approach as is used in elastoplasticity [21]. Crucial in this approach is the definition of the elastic trial step. In the following, we first examine the 1D setup and then propose a new formulation for the trial step based on this. Existing alternative formulations are also reported for reference.

2.2 1D description for planar surfaces

We first examine the friction formulation on 1D, planar surfaces, since this serves as a motivation for our proposed new friction formulation, which is discussed in Sec. 2.5. In 1D, the setup can be described by the behavior shown in Fig. 1. The friction state is characterized by a point on

³Here, the coefficient of sticking friction is considered equal to the coefficient of sliding friction.

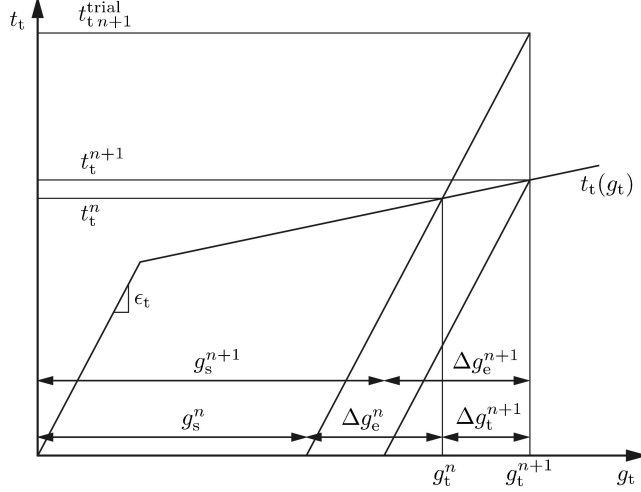


Figure 1: Description of 1D friction on planar surfaces.

the $t_t(g_t)$ curve which is either in the state of sticking or sliding. At time n the corresponding slip and traction are g_t^n and t_t^n . The former decomposes into an inelastic (sliding) and an elastic (sticking) component, written as

$$g_t^n = g_s^n + \Delta g_e^n . \quad (6)$$

The traction at step n can then be written as

$$t_t^n = \epsilon_t (g_t^n - g_s^n) . \quad (7)$$

We now consider an advancement of the tangential slip from step n to $n + 1$ as

$$g_t^{n+1} = g_t^n + \Delta g_t^{n+1} . \quad (8)$$

According to Fig. 1, the trial traction, for a linear elastic penalty regularization, is then given by

$$t_{t\,n+1}^{trial} = t_t^n + \epsilon_t (g_t^{n+1} - g_t^n) , \quad (9)$$

or equivalently

$$t_{t\,n+1}^{trial} = \epsilon_t (g_t^{n+1} - g_s^n) . \quad (10)$$

2.3 3D surface description

As a precursor to the formulation of 3D friction on general surfaces, we first summarize briefly the description of 3D surfaces. A 3D surface, like the boundary $\partial\mathcal{B}$ of body \mathcal{B} , can be described by the mapping

$$\mathbf{x} = \mathbf{x}(\boldsymbol{\xi}) , \quad \boldsymbol{\xi} \in \mathcal{P} , \quad (11)$$

that maps a point $\boldsymbol{\xi} = \{\xi^1, \xi^2\}$ lying in the 2D parameter space \mathcal{P} to the surface point $\mathbf{x} \in \partial\mathcal{B}$. For the formulation of contact between two bodies \mathcal{B}_1 and \mathcal{B}_2 , the normal distance and relative tangential distance between surface points typically needs to be evaluated. Therefore the closest projection point \mathbf{x}_p of a given surface point $\mathbf{x}_k \in \partial\mathcal{B}_k$ ($k = 1, 2$) onto the neighboring surface $\partial\mathcal{B}_\ell$ ($\ell = 2, 1$) needs to be determined. This point is defined by the parametric coordinate $\boldsymbol{\xi}_p$, i.e. $\mathbf{x}_p = \mathbf{x}_\ell(\boldsymbol{\xi}_p)$. The surface $\partial\mathcal{B}_\ell$ at \mathbf{x}_p is characterized by the co-variant tangent vectors

$$\mathbf{a}_\alpha^p := \left. \frac{\partial \mathbf{x}_\ell}{\partial \xi^\alpha} \right|_{\boldsymbol{\xi}_p} , \quad \alpha = 1, 2 , \quad (12)$$

the contra-variant tangent vectors

$$\mathbf{a}_p^\alpha = a_p^{\alpha\beta} \mathbf{a}_\beta^p, \quad [a_p^{\alpha\beta}] = [a_{\alpha\beta}^p]^{-1}, \quad a_{\alpha\beta}^p = \mathbf{a}_\alpha^p \cdot \mathbf{a}_\beta^p, \quad (13)$$

and the normal vector

$$\mathbf{n}_p := \frac{\mathbf{a}_1^p \times \mathbf{a}_2^p}{\|\mathbf{a}_1^p \times \mathbf{a}_2^p\|}. \quad (14)$$

With this, the contact traction acting at $\mathbf{x}_k \in \partial\mathcal{B}_k$ is decomposed as

$$\mathbf{t}_c = p \mathbf{n}_p - \mathbf{t}_t, \quad \text{with} \quad \mathbf{t}_t = t_t^\alpha \mathbf{a}_\alpha^p, \quad (15)$$

where t_t^1, t_t^2 and p denote the traction components in the $\{\mathbf{a}_1^p, \mathbf{a}_2^p, \mathbf{n}_p\}$ basis, taken here from the neighboring surface $\partial\mathcal{B}_\ell$. The minus sign is motivated in Sec. 2.5. With the definition of the tangent vectors, the coordinates of the projection point, ξ_p^α , can be computed from the two nonlinear equations

$$(\mathbf{x}_p - \mathbf{x}_k) \cdot \mathbf{a}_\alpha^p = 0, \quad \alpha = 1, 2, \quad (16)$$

e.g. see [1]. During contact the projection point \mathbf{x}_p moves across the surface $\partial\mathcal{B}_\ell$, which implies a change in coordinates ξ_p^α . From time step n to $n+1$ this advancement is expressed as

$$\xi_{p n+1}^\alpha = \xi_{p n}^\alpha + \Delta \xi_{p n+1}^\alpha. \quad (17)$$

For a penalty regularization we can then split $\xi_{p n}^\alpha$ into inelastic (sliding) and elastic (sticking) components, i.e.

$$\xi_{p n}^\alpha = \xi_{s n}^\alpha + \Delta \xi_{e n}^\alpha. \quad (18)$$

Thus, space \mathcal{P} simply takes over the role of the 1D plane considered in Fig. 1. Here we note that $\xi_{p n}^\alpha$ and $\xi_{s n}^\alpha$ mark absolute positions while $\Delta \xi_{e n}^\alpha$ marks a signed relative distance on \mathcal{P} . As long as no contact occurs we set $\Delta \xi_{e n}^\alpha = 0$ and $\xi_{s n}^\alpha = \xi_{p n}^\alpha$.

Here we consider that $\Delta \xi_e^n = \{\Delta \xi_e^{n1}, \Delta \xi_e^{n2}\}$ is small, i.e. due to a large penalty parameter ϵ_t . This implies that the orientation of the tangent plane of $\partial\mathcal{B}_\ell$ is approximately equal at $\mathbf{x}_\ell(\xi_p^n)$ and $\mathbf{x}_\ell(\xi_s^n)$. This also implies that $\mathbf{x}_\ell(\xi_s^n)$ travels on the same path as $\mathbf{x}_\ell(\xi_p^n)$. In general, for large $\Delta \xi_e^n$, the tangent plane can change substantially between $\mathbf{x}_\ell(\xi_p^n)$ and $\mathbf{x}_\ell(\xi_s^n)$ and the two points will not travel on the same paths.

Remark: The position of Greek indices indicates co-variant and contra-variant variables. For all other indices ($p, n, n+1, \dots$) their position has no meaning and they are placed wherever convenient.

2.4 Existing 3D trial traction formulations

Laursen considers the following formulation for the tangential trial tractions (see [9] p. 160)

$$\mathbf{t}_{t n+1}^{\text{trial}} = \left(t_{t\alpha}^n + \epsilon_t a_{\alpha\beta}^{p n+1} (\xi_{p n+1}^\beta - \xi_{p n}^\beta) \right) \mathbf{a}_{p n+1}^\alpha. \quad (19)$$

A slight inconsistency is present in this formulation since the co-variant traction component at step n , i.e. $t_{t\alpha}^n = \mathbf{t}_t^n \cdot \mathbf{a}_{p n}^\alpha$, does not strictly belong to the basis $\mathbf{a}_{p n+1}^\alpha$. Two approximation errors result from this: (a) the change in direction between $\mathbf{a}_{p n}^\alpha$ and $\mathbf{a}_{p n+1}^\alpha$ is not accounted for in the terms associated with $t_{t\alpha}^n$ and $\xi_{p n}^\beta$. This is fine for small Δt , where the orientation of the tangent plane does not change between $\mathbf{x}_\ell(\xi_p^n)$ and $\mathbf{x}_\ell(\xi_p^{n+1})$. (b) The surface stretch between $\mathbf{a}_{p n}^\alpha$ and $\mathbf{a}_{p n+1}^\alpha$ is not correctly accounted for in \mathbf{t}_t^n . The last inconsistency can be fixed if one considers $t_{t\alpha}^n = \epsilon_t a_{\alpha\beta}^{p n+1} \Delta \xi_{e n}^\beta$. In that case we obtain the variant

$$\mathbf{t}_{t n+1}^{\text{trial}} = \epsilon_t (\xi_{p n+1}^\alpha - \xi_{s n}^\alpha) \mathbf{a}_{\alpha n+1}^p, \quad (20)$$

analogously to Eq. (10). Due to the first inconsistency, the tangent that is obtained for an elastic sticking step is not symmetric. This motivates the formulation proposed in the following section.

For C^0 -surface discretizations the tangent directions jump between elements, which motivated the formulations of [22] and [23]. The formulation of [22] can be shown to be equal to the formulation of Wrighers [10],

$$\mathbf{t}_{t_{n+1}}^{\text{trial}} = \mathbf{t}_t^n + \epsilon_t (\xi_{p_{n+1}}^\alpha - \xi_{p_n}^\alpha) \mathbf{a}_{\alpha_{n+1}}^p. \quad (21)$$

This formulation is affected by similar inconsistencies noted above: (a) direction $\mathbf{a}_{\alpha_{n+1}}^p$ does not correspond to $\xi_{p_n}^\alpha$; (b) the extra stretch from the update $n \rightarrow n+1$ is not accounted for in the first term. [23] considers the same formulation as Laursen's, but in terms of the nominal traction $\mathbf{T}_t = \mathbf{t}_t da/dA$. To account for the C^0 surface deficiencies, they consider the update

$$\Delta \xi_{p_{n+1}}^\alpha = \left(\mathbf{x}_\ell^n(\xi_p^{n+1}) - \mathbf{x}_\ell^n(\xi_p^n) \right) \cdot \mathbf{a}_{p_n}^\alpha. \quad (22)$$

2.5 Proposed 3D trial traction formulation

In analogy to expression (7), the proposed new formulation is constructed by considering the following penalty regularization

$$\mathbf{t}_t^n = \epsilon_t \left(\mathbf{x}_\ell^n(\xi_p^n) - \mathbf{x}_\ell^n(\xi_s^n) \right), \quad (23)$$

i.e. we consider a linear elastic relation between $\Delta \mathbf{x}_e^n := \mathbf{x}_\ell^n(\xi_p^n) - \mathbf{x}_\ell^n(\xi_s^n)$ and \mathbf{t}_t^n . We note that this formulation can be connected to an elastic potential defined on $\Delta \mathbf{x}_e$. At step $n+1$ the traction of Eq. (23) updates to

$$\mathbf{t}_{t_n}^{\text{up}} = \epsilon_t \left(\mathbf{x}_\ell^{n+1}(\xi_p^n) - \mathbf{x}_\ell^{n+1}(\xi_s^n) \right). \quad (24)$$

This update accounts for rigid surface rotations, as well as surface stretches. The latter thus accounts for a desired additional loading of the elastic spring. The proposed new trial traction formulation now consists of

$$\mathbf{t}_{t_{n+1}}^{\text{trial}} = \mathbf{t}_{t_n}^{\text{up}} + \epsilon_t \left(\mathbf{x}_\ell^{n+1}(\xi_p^{n+1}) - \mathbf{x}_\ell^{n+1}(\xi_p^n) \right), \quad (25)$$

or equivalently

$$\mathbf{t}_{t_{n+1}}^{\text{trial}} = \epsilon_t \left(\mathbf{x}_\ell^{n+1}(\xi_p^{n+1}) - \mathbf{x}_\ell^{n+1}(\xi_s^n) \right). \quad (26)$$

These expressions are analogous to the 1D case, see Eqs. (9) and (10). A visualization of the proposed approach is shown in Fig. 2. Note that typically both $\Delta \xi_p^{n+1} = \xi_p^{n+1} - \xi_p^n$ and $\Delta \xi_e^n = \xi_p^n - \xi_s^n$ are going to be very small (since the time step Δt and ϵ_t^{-1} are small), such that $\mathbf{t}_{t_{n+1}}^{\text{trial}}$ lies very close to the tangent plane of $\partial \mathcal{B}_\ell^{n+1}$ at \mathbf{x}_p^{n+1} . For $\Delta t \rightarrow 0$, expression (26) is equivalent to the formulations of Sec. 2.4, as is formally shown in appendix A.

Remark 1: For large Δt , the proposed, as well as the formulations of Sec. 2.4, become inaccurate. While the new formulation removes some of the inconsistencies of the previous formulations, it is still only approximate and therefore also contains some errors that are related to the surface curvature: For curved surfaces the difference $\mathbf{x}_\ell^{n+1}(\xi_p^{n+1}) - \mathbf{x}_\ell^{n+1}(\xi_p^n)$ does not properly capture the additional length and current direction of the sliding path. A refinement to this end has been proposed by [24].

Remark 2: Expression (26) can be somewhat 'improved' if we project $\mathbf{t}_{t_{n+1}}^{\text{trial}}$ into the tangent plane of $\partial \mathcal{B}_\ell^{n+1}$. In that case we can also replace $\mathbf{x}_\ell^{n+1}(\xi_p^{n+1})$ by \mathbf{x}_k^{n+1} so that we finally get

$$\mathbf{t}_{t_{n+1}}^{\text{trial}} = \epsilon_t \left(\mathbf{I} - \mathbf{n}_p^{n+1} \otimes \mathbf{n}_p^{n+1} \right) \left(\mathbf{x}_k^{n+1} - \mathbf{x}_\ell^{n+1}(\xi_s^n) \right). \quad (27)$$

For small time steps, as they are considered in the later examples, only irrelevant differences have been found between expressions (27) and (26).

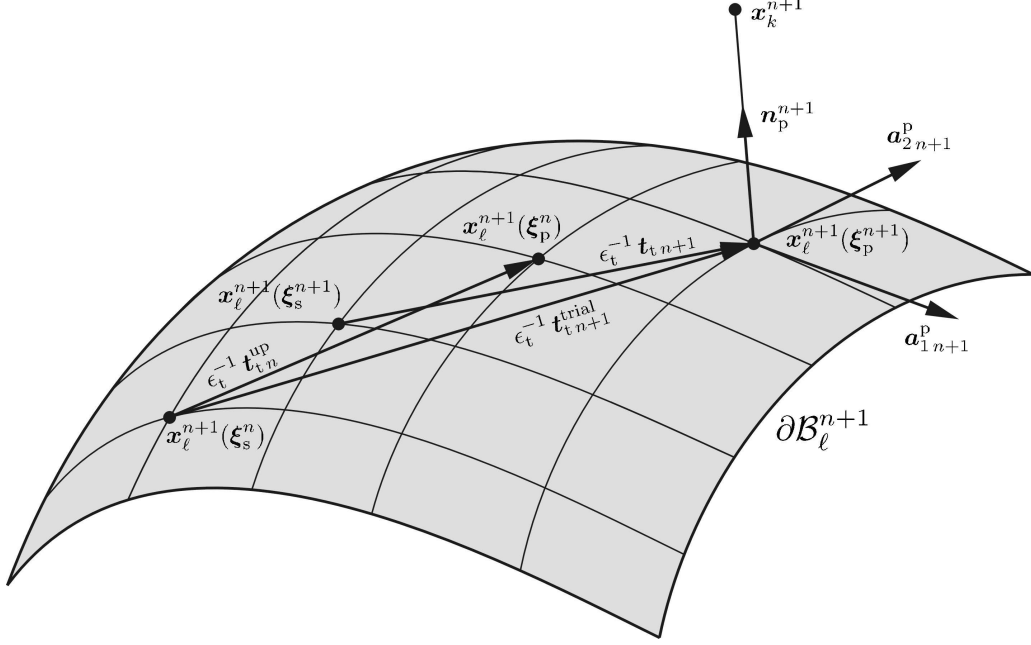


Figure 2: Description of 3D friction on curved surfaces parameterized by surface coordinates ξ^α and tangent vectors \mathbf{a}_α ($\alpha = 1, 2$). The traction resisting the tangential motion of \mathbf{x}_k is $-\mathbf{t}_t$, while $+\mathbf{t}_t$ are the tractions acting on the projection point $\mathbf{x}_p = \mathbf{x}_\ell(\boldsymbol{\xi}_p)$.

2.6 Algorithmic treatment

We now discuss the formulation of the friction algorithm based on (26). The algorithm is formulated within the two-half-pass approach [1]: for a surface point $\mathbf{x}_k \in \partial\mathcal{B}_k$ the projection point $\mathbf{x}_p \in \partial\mathcal{B}_\ell$ ($\ell \neq k$) is computed according to the above procedure. The traction acting at \mathbf{x}_k is then $-\mathbf{t}_t$ (see Fig. 2). The procedure is carried out equivalently for both surfaces $k = 1, 2$. The friction algorithm is based on a predictor-corrector approach to enforce slip criterion (2), see [10]. First, f_s is evaluated for the trial state, giving $f_s^{\text{trial}} = f_s(\mathbf{t}_{tn+1}^{\text{trial}})$. If $f_s^{\text{trial}} < 0$ we are in a sticking state with $\mathbf{t}_t^{n+1} = \mathbf{t}_{tn+1}^{\text{trial}}$ and $\xi_{sn+1}^\alpha = \xi_{sn}^\alpha$. If $f_s^{\text{trial}} \leq 0$ we have to enforce $f_s = 0$ considering the evolution law for the inelastic slip coordinate $\boldsymbol{\xi}_s$. This law can be obtained by examining the dissipation (energy loss per time and area) during friction, which is given by

$$\mathcal{D} = \mathbf{t}_t \cdot \mathcal{L}\mathbf{g}_s, \quad (28)$$

where

$$\mathcal{L}\mathbf{g}_s = \dot{\xi}_s^\alpha \mathbf{a}_\alpha^s, \quad \text{with } \mathbf{a}_\alpha^s = \left. \frac{\partial \mathbf{x}_\ell}{\partial \xi^\alpha} \right|_{\boldsymbol{\xi}_s}, \quad (29)$$

is the Lie derivative of the inelastic slip vector \mathbf{g}_s . Here \mathbf{a}_α^s is the co-variant tangent vector at $\boldsymbol{\xi}_s$. Invoking the principle of maximum dissipation [10] one can show that $\mathcal{L}\mathbf{g}_s \parallel \partial f_s / \partial \mathbf{t}_t$, i.e. we find the following evolution law for the inelastic slip

$$\mathcal{L}\mathbf{g}_s = \gamma \mathbf{n}_t, \quad \mathbf{n}_t := \frac{\partial f_s}{\partial \mathbf{t}_t} = \frac{\mathbf{t}_t}{\|\mathbf{t}_t\|}. \quad (30)$$

Inserting eq. (29) and contracting with \mathbf{a}_s^α , the contra-variant tangent vector at $\boldsymbol{\xi}_s$, we find

$$\dot{\xi}_s^\alpha = \gamma \mathbf{n}_t \cdot \mathbf{a}_s^\alpha. \quad (31)$$

Using implicit Euler, this is then discretized as

$$\xi_{s_{n+1}}^\alpha = \xi_{s_n}^\alpha + \Delta \xi_{s_{n+1}}^\alpha, \quad \text{with } \Delta \xi_{s_{n+1}}^\alpha \approx \Delta \gamma_{n+1} \mathbf{n}_t^{n+1} \cdot \mathbf{a}_{s_{n+1}}^\alpha. \quad (32)$$

Mapping ξ_s to surface $\partial \mathcal{B}_\ell$ at $n+1$, we now obtain the update

$$\mathbf{x}_\ell^{n+1}(\xi_s^{n+1}) = \mathbf{x}_\ell^{n+1}(\xi_s^n) + \Delta \mathbf{x}_\ell^{n+1}, \quad (33)$$

with

$$\Delta \mathbf{x}_\ell^{n+1} \approx \Delta \xi_{s_{n+1}}^\alpha \mathbf{a}_{\alpha_{n+1}}^s = \Delta \gamma_{n+1} \mathbf{n}_t^{n+1} \quad (34)$$

due to eq. (32.2). The traction at $n+1$, given as

$$\mathbf{t}_t^{n+1} = \epsilon_t (\mathbf{x}_\ell^{n+1}(\xi_p^{n+1}) - \mathbf{x}_\ell^{n+1}(\xi_s^{n+1})) \quad (35)$$

according to eq. (23), now becomes

$$\begin{aligned} \mathbf{t}_t^{n+1} &= \epsilon_t (\mathbf{x}_\ell^{n+1}(\xi_p^{n+1}) - \mathbf{x}_\ell^{n+1}(\xi_s^n) - \Delta \gamma_{n+1} \mathbf{n}_t^{n+1}) \\ &= \mathbf{t}_{t_{n+1}}^{\text{trial}} - \epsilon_t \Delta \gamma_{n+1} \mathbf{n}_t^{n+1}. \end{aligned} \quad (36)$$

This can be expanded into

$$\mathbf{n}_t^{n+1} (\|\mathbf{t}_t^{n+1}\| + \epsilon_t \Delta \gamma_{n+1}) = \mathbf{n}_{t_{n+1}}^{\text{trial}} \|\mathbf{t}_{t_{n+1}}^{\text{trial}}\|, \quad (37)$$

which implies

$$\mathbf{n}_t^{n+1} = \mathbf{n}_{t_{n+1}}^{\text{trial}} \quad (38)$$

and

$$\|\mathbf{t}_t^{n+1}\| = \|\mathbf{t}_{t_{n+1}}^{\text{trial}}\| - \epsilon_t \Delta \gamma_{n+1}. \quad (39)$$

Enforcing $f_s^{n+1} = 0$ now gives

$$\Delta \gamma_{n+1} = \frac{\|\mathbf{t}_{t_{n+1}}^{\text{trial}}\| - \mu p_{n+1}}{\epsilon_t}. \quad (40)$$

Inserting this expression into eq. (36) correctly returns Coulomb's law

$$\mathbf{t}_t^{n+1} = \mu p_{n+1} \mathbf{n}_t^{n+1}. \quad (41)$$

The friction algorithm following from these equations is summarized in table 1. The algorithm is embedded within the contact algorithm employed for the discretized system (see Sec. 3). For the two-half-pass approach the algorithm is applied to every contact point $\mathbf{x}_k \in \partial \mathcal{B}_k$ for both surfaces ($k = 1, 2$). The current surface descriptions \mathbf{x}_k^{n+1} and \mathbf{x}_ℓ^{n+1} are provided through the global Newton iteration.

Note, that since $\mathbf{a}_{s_{n+1}}^\alpha$ depends on $\xi_{s_{n+1}}^\alpha$, update (32) is a nonlinear equation that can for example be solved by a local Newton iteration. Since $\Delta \xi_e^{n+1}$ is considered small, we can replace $\mathbf{a}_{s_{n+1}}^\alpha$ by $\mathbf{a}_{p_{n+1}}^\alpha$ inside (32), as is done in table 1. As a simple alternative one can also take $\mathbf{a}_{s_{n+1}}^\alpha$ from the previous step of the global Newton iteration. If no contact occurs we set $\mathbf{t}_{t_{n+1}} = \mathbf{0}$ and $\xi_{s_{n+1}}^\alpha = \xi_{p_{n+1}}^\alpha$.

Remark: The accuracy of the friction algorithm depends on the step size $\Delta \gamma$ (due to Δt) that affects the implicit Euler approximation in (32) and the traction formulation of Sec. 2.5 (see remarks there). For quasi-static problems the ‘time’ step $n \rightarrow n+1$ is set by the loading steps applied to the system. In the examples of Sec. 4, those steps have been considered sufficiently small, and their influence on the accuracy is investigated.

1.	<u>Given, starting values</u>	
	$\boldsymbol{\xi}_p^n, \boldsymbol{\xi}_s^n$	previous coordinates of the projection and sliding points
	\boldsymbol{x}_k^{n+1}	current position of the surface point $\boldsymbol{x}_k \in \partial\mathcal{B}_k$
	$\boldsymbol{x}_\ell^{n+1} = \boldsymbol{x}_\ell^{n+1}(\boldsymbol{\xi})$	current surface description of $\partial\mathcal{B}_\ell$
	$\boldsymbol{\xi}_p^{n+1}, p_{n+1}$	current projection point coordinate and contact pressure for point \boldsymbol{x}_k^{n+1} (both obtained from a normal contact algorithm)
2.	<u>Elastic predictor step</u>	
	$\boldsymbol{t}_{tn+1}^{\text{trial}} = \epsilon_t (\boldsymbol{x}_\ell^{n+1}(\boldsymbol{\xi}_p^{n+1}) - \boldsymbol{x}_\ell^{n+1}(\boldsymbol{\xi}_s^n))$	
3.	<u>Check slip criterion</u>	
	$f_{sn+1}^{\text{trial}} = \ \boldsymbol{t}_{tn+1}^{\text{trial}}\ - \mu p_{n+1}$	
	if $f_{sn+1}^{\text{trial}} \leq 0$: sticking state; $\Delta\gamma_{n+1} = 0$	
	if $f_{sn+1}^{\text{trial}} > 0$: sliding state; $\Delta\gamma_{n+1} = f_{sn+1}^{\text{trial}}/\epsilon_t$	
4.	<u>Inelastic corrector step</u>	
	$\boldsymbol{\xi}_{sn+1}^\alpha = \boldsymbol{\xi}_s^\alpha + \Delta\gamma_{n+1} \boldsymbol{n}_t^{n+1} \cdot \boldsymbol{a}_{pn+1}^\alpha$	with $\boldsymbol{n}_t^{n+1} = \frac{\boldsymbol{t}_{tn+1}^{\text{trial}}}{\ \boldsymbol{t}_{tn+1}^{\text{trial}}\ }$
	$\boldsymbol{t}_t^{n+1} = \boldsymbol{t}_{tn+1}^{\text{trial}} - \epsilon_t \Delta\gamma_{n+1} \boldsymbol{n}_t^{n+1}$	

Table 1: Predictor-corrector algorithm for the computation of the tangential contact force, \boldsymbol{t}_t , at the surface point $\boldsymbol{x}_k \in \partial\mathcal{B}_k$. The algorithm is employed independently on both surfaces ($k = 1, 2$).

3 Finite element discretization

This section briefly summarizes the spatial finite element discretization of the model equations of Sec. 2. Two approaches are discussed: The classical full-pass approach, as it is for example considered in [3] and [4], and the two-half-pass approach presented in [1]. For the full-pass approach, we loop over the elements of one surface (the designated slave surface), denoted $\partial_c\mathcal{B}_k$ ($k = 1$ or $k = 2$), to compute the elemental contact force vectors

$$\mathbf{f}_{ck}^e = - \int_{\Gamma_k^e} \mathbf{N}_k^T \boldsymbol{t}_k \, da_k, \quad \mathbf{f}_{c\ell}^e = \int_{\Gamma_k^e} \mathbf{N}_\ell^T \boldsymbol{t}_k \, da_k, \quad (42)$$

acting on element $\Gamma_k^e \subset \partial_c\mathcal{B}_k^h$ and partially on some elements $\Gamma_\ell^e \subset \partial_c\mathcal{B}_\ell^h$ ($\ell \neq k$). Here \mathbf{N}_k and \mathbf{N}_ℓ are the arrays containing the nodal shape function of the elements. In this paper Hermite [12] and NURBS-based [25] shape functions are used for the contact surface interpolation. For the two-half-pass approach we loop over both contact surfaces $\partial_c\mathcal{B}_k$ ($k = 1$ and $k = 2$) to compute the elemental contact force vector⁴

$$\mathbf{f}_{ck}^e = - \int_{\Gamma_k^e} \mathbf{N}_k^T \boldsymbol{t}_k \, da_k, \quad (43)$$

⁴The two-half-pass version considered here is denoted ‘class P’ in [1].

acting on element $\Gamma_k^e \subset \partial_c \mathcal{B}_k^h$. In both cases \mathbf{t}_k is given by eq. (15). The corresponding global virtual work contributions are, for the full-pass

$$G_c = - \int_{\partial \mathcal{B}_k} \delta \boldsymbol{\varphi}_k \cdot \mathbf{t}_k da_k + \int_{\partial \mathcal{B}_\ell} \delta \boldsymbol{\varphi}_\ell \cdot \mathbf{t}_k da_k, \quad k = 1, \ell = 2, \text{ or } k = 2, \ell = 1, \quad (44)$$

and for the two-half-pass

$$G_c = - \sum_{k=1}^2 \int_{\partial \mathcal{B}_k} \delta \boldsymbol{\varphi}_k \cdot \mathbf{t}_k da_k, \quad (45)$$

where $\delta \boldsymbol{\varphi}_k$ denotes the virtual deformation of body \mathcal{B}_k . The conceptual difference between the two approaches is illustrated in Fig. 3. For the full-pass approach, two variants are possible

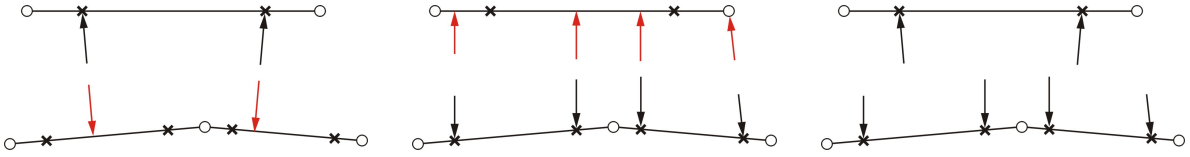


Figure 3: Full-pass and two-half-pass approaches: Full-pass with upper surface as slave (left); full-pass with lower surface as slave (middle); two-half-pass (right). Black forces: quadrature point entries in $\mathbf{f}_{c_k}^e$; red forces: quadrature point entries in $\mathbf{f}_{c_\ell}^e$.

as the figure shows. It is emphasized that for the two-half-pass, contrary to the full-pass, the contact tractions are computed separately for the two surfaces and are therefore, in general, not in exact equilibrium. This inaccuracy is an error measure of the two-half-pass algorithm. In the examples we have studied so far we have found that this error is of the same order as the discretization error. Therefore, the error vanishes as the discretization parameters approach the exact continuum limit. This is shown in detail for the examples in Secs. 4.2 and 4.3. The FE solution algorithm for the two-half-pass approach follows the algorithm given in [1], where step 2 is now given by table 2. To distinguish the states of contact (on/off) and friction (stick/slip), active sets are needed for both surfaces. In case of the full-pass algorithm only one surface loop and corresponding active set is needed. But additionally, the contribution $\mathbf{f}_{c_\ell}^e$ and associated stiffness terms $\mathbf{k}_{c_{\ell k}}^e$ and $\mathbf{k}_{c_{\ell \ell}}^e$ have to be computed, see appendix B. In all cases, the numerical integration over Γ_k^e is carried out in parameter space \mathcal{P} , over the master element defined by $\xi^\alpha \in [-1, 1]$. For the accurate integration, which is crucial for elements containing contact state changes, a large number of quadrature points is considered here for simplicity.⁵ The area transformation between master configuration and current configuration is given by

$$da_k = J_k d\boldsymbol{\square}, \quad (46)$$

where $d\boldsymbol{\square} := d\xi^1 d\xi^2$ and $J_k := \sqrt{\det a_{\alpha\beta}}$, $a_{\alpha\beta} = \mathbf{a}_\alpha^k \cdot \mathbf{a}_\beta^k$, and where \mathbf{a}_α^k are the tangent vectors of $\partial \mathcal{B}_k$ at \mathbf{x}_k .

An important aspect of the two-half-pass approach is its computational stability during challenging contact simulations. In the current formulation the contact constraints (impenetrability and sticking) are enforced at the quadrature level of integrals (42) and (43) using a penalty regularization. This can lead to a loss of numerical stability due to over-constraining of the formulation, especially if many quadrature points are considered, and especially in the two-half-pass case, where twice as many constraints are needed to characterize the tractions independently on the two surfaces (see Fig. 3). Over-constraining is the result of trying to satisfy too many

⁵An alternative is to consider segmentation techniques to subdivide the contact elements into easily-integrable regions [26], although, here, this would require the accurate determination of the state boundary.

At each load or time step $n \rightarrow n + 1$:

For each surface $\partial\mathcal{B}_k$ ($k = 1, 2$): loop over the active contact elements Γ_k^e to compute force \mathbf{f}_{ck}^e (43) and associated stiffness terms $\mathbf{k}_{ckk}^e, \mathbf{k}_{ckl}^e$ (64) by numerical quadrature; therefore, at each quadrature point \mathbf{x}_k :

i. closest point computation

1. solve (16) with Newton's method to obtain the coordinates $\boldsymbol{\xi}_p$ of the closest projection point $\mathbf{x}_p \in \partial\mathcal{B}_\ell$ of \mathbf{x}_k
2. evaluate the normal contact distance g_n and corresponding direction \mathbf{n}_p

ii. contact computation

if $g_n \geq 0$: set \mathbf{t}_k and corresponding gradients to zero; set $\boldsymbol{\xi}_s = \boldsymbol{\xi}_p$

if $g_n < 0$:

1. evaluate the normal contact force $\mathbf{t}_n = p \mathbf{n}_p$ based on Eq. (66)
2. evaluate the tangential contact force \mathbf{t}_t from the algorithm of table 1
3. obtain the coordinates $\boldsymbol{\xi}_s$ from the algorithm of table 1
4. compute the gradients $\frac{\partial \mathbf{t}_k}{\partial \mathbf{u}_k^e}$ and $\frac{\partial \mathbf{t}_k}{\partial \mathbf{u}_\ell^e}$, according to appendix B

Table 2: The two-half-pass algorithm for frictional contact.

constraints with too few degrees-of-freedom. This leads to *surface locking* [27; 5] and the failure of the LBB condition⁶. There are two principle ways to alleviate the problem: Firstly, by a reduction of the number of constraints, e.g. through a nodal patterning approach, as is considered by [5] and [6] for the earlier formulation of [2]. The second possibility, pursued here, is to satisfy the constraints approximately instead of exactly, e.g. by using moderate penalty parameters. This is motivated by the fact that the discretized contact problem is anyway only solved approximately. All the examples that we have considered so far indicate that the constraints can be solved to the same order of accuracy as the discretization error without running into numerical ill-conditioning resulting from over-constraining. This is shown in detail in the example of Sec. 4.3. This property of our approach stands in contrast to a result of [6], which indicates that a two-pass penalty regularization without constraint reductions either leads to severe inaccuracy or over-constraining. We believe that the main reason why our method can get accurate and stable solutions lies in omitting any enforcement of traction continuity from the formulation and relying on the fact, also noted in [2], that traction continuity is recovered as the mesh is refined. This omission effectively imposes less restrictions on our solution. In the case of inequality constraints the situation is somewhat less critical, as redundant constraints can, in theory, release and become inactive. Exploiting this property is therefore a third option. This has been considered successfully in the context of infinitesimal, frictionless contact in [28].

4 Numerical examples

This section discusses four examples that illustrate the symmetry (Sec. 4.1), the influence of the model parameters (Sec. 4.2), the convergence behavior (Sec. 4.3) and the 3D behavior (Sec. 4.4)

⁶Ladyzhenskaia-Babuška-Brezzi condition e.g. see [27] for the case of contact.

of the proposed new contact algorithm.

4.1 A symmetric test case (for frictional contact)

The first example considers a simple symmetric test case, that is useful for testing the two-half-pass algorithm for frictional contact. The problem setup, shown in Fig. 4, consists of two half-cylinders with radius L_0 that are pressed together by applying the displacement components $\bar{u}_y = -\bar{u}$ and $\bar{u}_x = \bar{u}/2$ to the top boundary of the upper cylinder. The perfect symmetry of

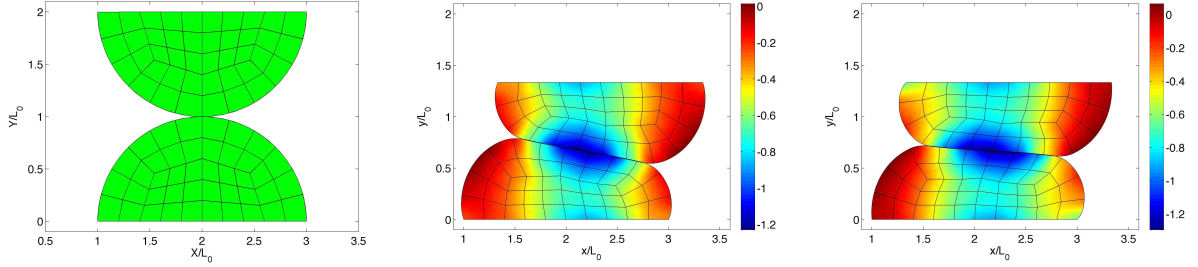


Figure 4: Test case: Undeformed configuration (left); deformation for $\mu = 0.1$ (middle); deformation for $\mu = 0.6$ (right). The coloring shows the stress $I_1 = \text{tr } \boldsymbol{\sigma}$ normalized by E_0 .

the test case must result in the exact symmetry of the two half-passes, and the deformation and the contact traction must therefore be exactly equal on the two surfaces. Here, the two bodies are described by the Neo-Hookean material model [29]

$$\boldsymbol{\sigma} = \frac{\Lambda}{J} (\ln J) \mathbf{I} + \frac{G}{J} (\mathbf{F}\mathbf{F}^T - \mathbf{I}), \quad J = \det \mathbf{F}, \quad (47)$$

where \mathbf{F} is the deformation gradient and $\Lambda = 2G\nu/(1 - 2\nu)$ and $G = E/2/(1 + \nu)$ are the bulk and shear moduli (in the linear elastic regime). For both bodies the same material parameters $E = E_0$ and $\nu = 0.3$ are used. Parameter E_0 , along with dimension L_0 , are then used for the dimensional normalization of the problem. Contact is modeled by the penalty regularization considering a penalty parameter of $\epsilon_n = \epsilon_t = \epsilon = 100 E_0/L_0$ and the friction law of Coulomb (4). For accuracy and dense output of the contact tractions, 20 equidistant quadrature points are used to integrate (43). Q1CH contact elements based on C^1 -continuous Hermite interpolation are used for the computations [12; 17]. Two cases are considered: one for low μ , where full sliding occurs, and one for high μ , where full sticking occurs. Fig. 4 shows the deformation of the two cases for $\bar{u} = 2/3L_0$. The contact tractions for the two cases are shown in Fig. 5. The blue and red curves display the raw, i.e. quadrature point, data for the normal pressure $p = -\epsilon_n g_n$ and the tangential traction

$$t = \mathbf{t}_t \cdot \bar{\mathbf{a}}, \quad \bar{\mathbf{a}} = \frac{\mathbf{a}}{\|\mathbf{a}\|}, \quad \mathbf{a} = \frac{\partial \mathbf{x}}{\partial s}. \quad (48)$$

Here, S and s denote the surface coordinates in the reference and current configurations $\partial\mathcal{B}_0$ and $\partial\mathcal{B}$, and $\bar{\mathbf{a}}$ is the normalized surface tangent of $\partial\mathcal{B}$, considering that s runs from left to right along the contact surface. The corresponding black curves (dashed and solid) display the smoothed pressure and tangential traction according to the post-processing scheme of [17]. For the case of sliding ($\mu = 0.1$), the tangential traction $t(S)$ is (due to (4)) exactly proportional to the pressure $p(S)$. This is independent of the number of load steps. For the case of sticking ($\mu = 0.6$), two different numbers of load steps are considered to impose \bar{u} : $n_{\bar{u}} = 20$ and $n_{\bar{u}} = 200$. The latter yields a smoother result of the raw traction $t(S)$. For all cases, the difference of the

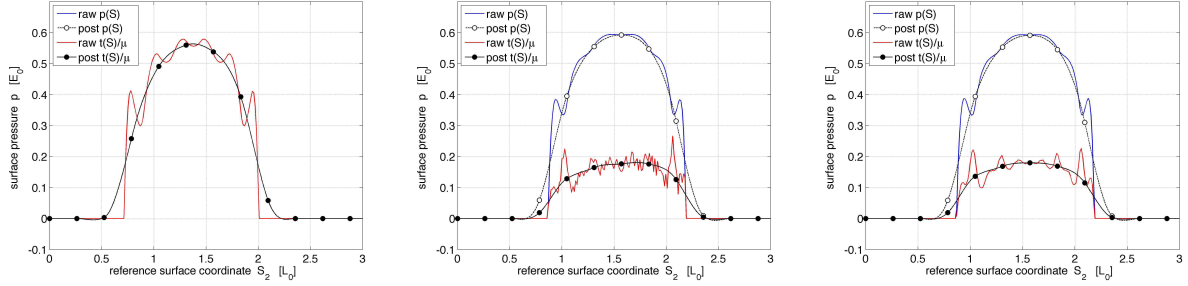


Figure 5: Test case: Contact tractions for $\mu = 0.1$ (left) and $\mu = 0.6$ with $n_{\bar{u}} = 20$ loadsteps (middle) and $n_{\bar{u}} = 200$ loadsteps (right). Here, $\epsilon = 100 E_0/L_0$.

normal and tangential tractions on the two surfaces lies at machine precision, as it should. Due to this traction equivalence, also the stress field within the two cylinders agrees to machine precision. This is shown in Fig. 6, where the deviation of $I_1 = \text{tr } \boldsymbol{\sigma}$ from its average value (of corresponding points on both bodies) is displayed. For comparison, Fig. 7 shows the same

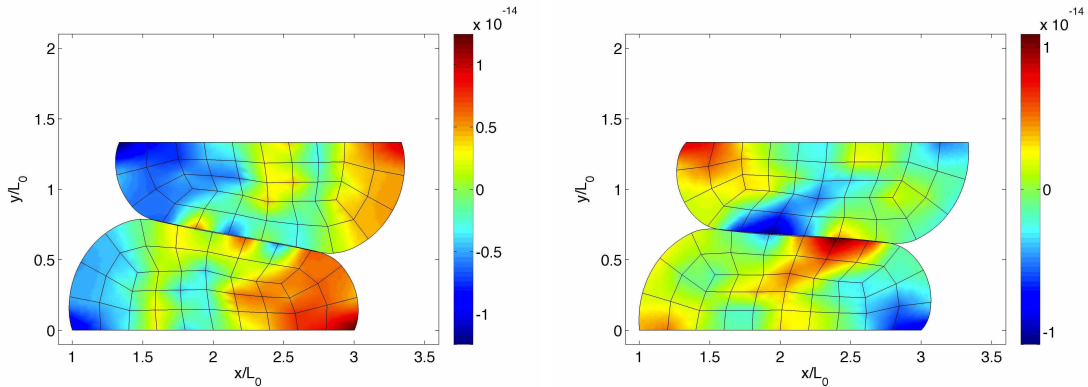


Figure 6: Test case: Inaccuracy in $I_1 = \text{tr } \boldsymbol{\sigma}$ (normalized by E_0) according to the two-half-pass algorithm for $\mu = 0.1$ (left) and $\mu = 0.6$ (right). This lies within machine precision. Here $n_{\bar{u}} = 100$.

results for the full-pass contact algorithm. This algorithm introduces a surface bias, which leads to a much higher error in the stress field (10^{-4} instead of 10^{-14}). The example demonstrates the merits of the unbiased two-half-pass algorithm.

4.2 2D ironing

4.2.1 Problem setup

The second example considers the ironing problem using the setup of [17]. The problem is used to carefully analyze the proposed new friction formulation and compare the two-half-pass algorithm with the full-pass algorithm. A half-cylinder (\mathcal{B}_1) with radius L_0 , is pressed into an elastic block (\mathcal{B}_2) and then moved horizontally across the block, as is shown in Fig. 8. The size of the block is $2L_0 \times 10L_0$. The bottom surface of the block is fixed, and periodic boundary conditions are applied at the two vertical boundaries. The Neo-Hooke material law (47) is used with $E_1 = 3E_0$, $E_2 = E_0$, and $\nu_1 = \nu_2 = 0.3$. The coefficient of sliding friction is taken as $\mu = 0.5$. The penalty parameters are taken as $\epsilon_n = \epsilon_t = \epsilon = 100 E_0/L_0$. As before,

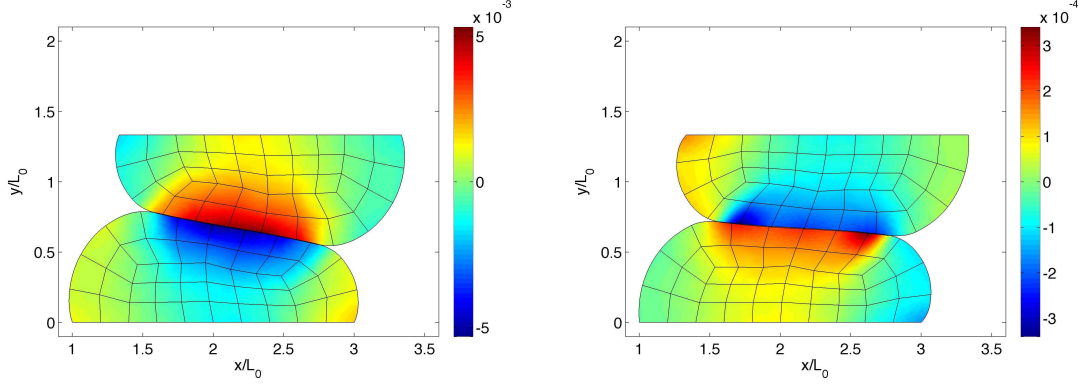


Figure 7: Test case: Inaccuracy in $I_1 = \text{tr } \boldsymbol{\sigma}$ (normalized by E_0) according to the full-pass algorithm for $\mu = 0.1$ (left) and $\mu = 0.6$ (right). The accuracy is more than 10^{10} times lower than in Fig. 6. Here $n_{\bar{u}} = 100$.

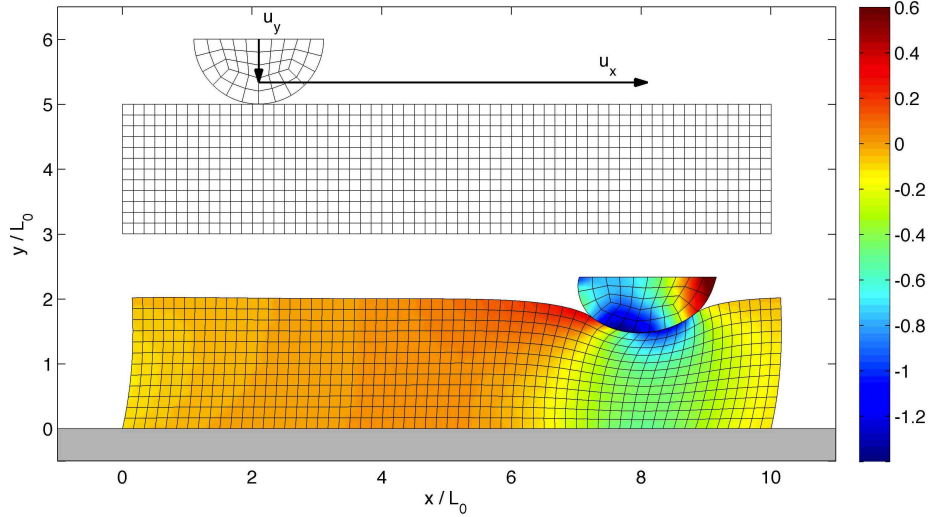


Figure 8: 2D frictional ironing: Initial configuration and deformed configuration. The coloring shows the stress $I_1 = \text{tr } \boldsymbol{\sigma}$ normalized by E_0 .

Hermite based, C^1 -continuous surface elements are used for the contact computations [12; 17], considering 20 equidistant quadrature points. The two-half-pass algorithm based on the friction formulation of table 1 is considered.

Fig. 9 shows a few snapshots of the solution during downward and sliding motion. The friction algorithm is considered active during both. Only sticking and no sliding occurs on the surface during the downward motion as is seen in the traction plots examined below.⁷ The spatial and temporal discretization of the problem is characterized by the numerical parameters m_k and $n_{\bar{u}}$. $n_{\bar{u}}$ denotes the number of loading steps to apply a prescribed displacement of $\bar{u} = L_0$. m_k characterizes the FE meshes: the number of elements of \mathcal{B}_1 and \mathcal{B}_2 is $n_{\text{el}1} = 21 m_1^2/32$ and $n_{\text{el}2} = 5 m_2^2$, respectively. Here parameter m_2 corresponds to the number of elements along $2L_0$ (the block height). The mesh for $m_1 = 8$ and $m_2 = 12$ is shown in Fig. 8. Otherwise we have considered the meshes for $m_1 = m_2 = m \in \{8, 16, 32\}$. As a reference result for the

⁷In the infinitesimal theory, the theoretical singularity of the tangential tractions (if present) necessitates a (small) sliding zone at the contact boundary [30]. In the present example, based on finite theory, such a zone has not been observed during downward or horizontal motion, even for very fine meshes.

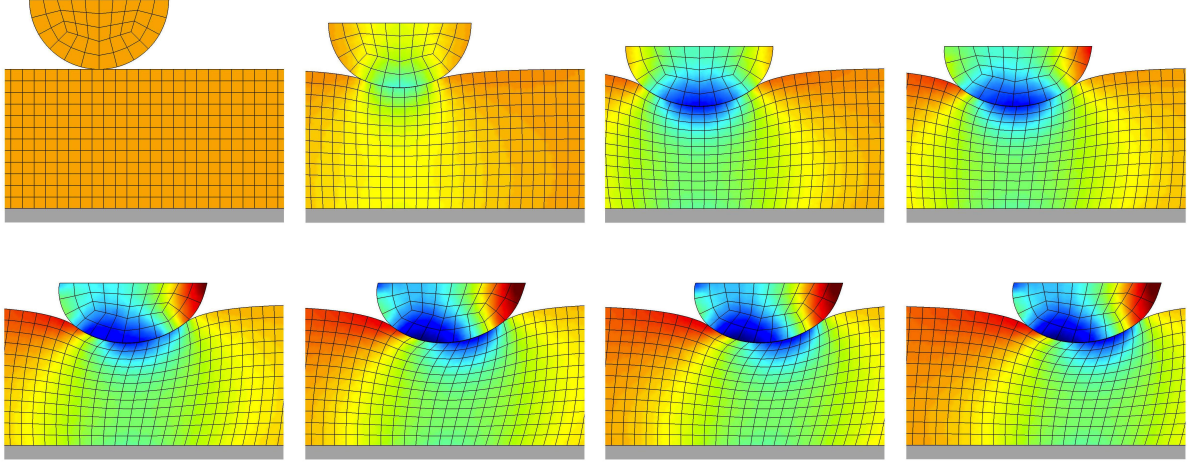


Figure 9: 2D frictional ironing: Deformation at $\bar{u}_x = 0$ and $\bar{u}_y = \{0, 1, 2\}L_0/3$ (downward motion; first three frames) and $\bar{u}_y = 2/3L_0$ and $\bar{u}_x = \{0, 1, 2, 3, 4, 5\}L_0/4$ (horizontal sliding motion; third to last frame). The coloring is the same as in Fig. 8.

following study, we have computed the tractions for the refined case $m = 64$, $n_{\bar{u}} = 1200$, and $\epsilon = 1000 E_0/L_0$, referred to as ‘exact’ solution in the following.

4.2.2 Net contact forces

Fig. 10 shows the global contact forces during sliding. Note that here in the nonlinear setting, $P_y \neq \mu P_x$, as one would expect for small deformations. The enlargements on the right hand side of Fig. 10 show the differences between the two-half-pass (2hp) and two full-pass (fp) solutions.⁸ Two different load step numbers, $n_{\bar{u}} = 20$ and $n_{\bar{u}} = 80$, are considered.⁹ As was already noted in Fig. 5, the refinement of the load stepping improves the results, especially for the 2hp algorithm. The reason for the improvement lies in the inaccurate determination of the initial contact point for coarse load stepping and the inaccurate determination of the trial traction that results from this. The inaccuracy therefore only affects the tangential contact traction and not the normal contact pressure. However, due to the large deformation, both P_x and P_y are affected by normal and tangential contact tractions. As the figure shows, the accuracy of the 2hp is comparable to the accuracy of the fp: It is better for P_x , worse for P_y , $n_{\bar{u}} = 20$ and similar for P_y , $n_{\bar{u}} = 80$. If one looks at the average of the 2hp forces (dashed green line), the 2hp result is always better than the fp results. It can also be concluded here, as in the other case we have studied so far, that the difference between the 2hp forces is of the same order as the error to the ‘exact’ solution. For a suitably refined load step (i.e. $n_{\bar{u}} = 80$), these errors are within 1% of the ‘exact’ solution.

4.2.3 Contact tractions during downward motion

Next, we examine the contact tractions during downward motion. The sliding motion is then examined in Sec. 4.2.4. Friction is considered in both motions. For the downward motion we now look at the

⁸We note again that the two full-pass solutions are taken from two separate runs, alternating the slave/master designation.

⁹During the preceding downward motion a very large number of load steps has been used, i.e. $n_{\bar{u}} = 1200$.

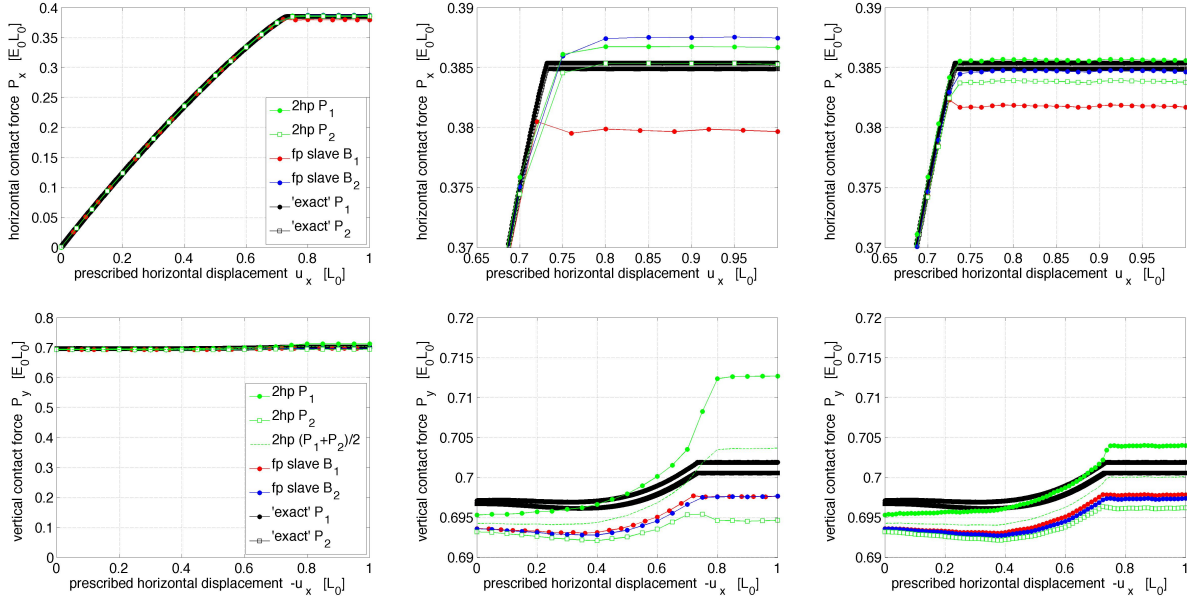


Figure 10: 2D frictional ironing: Net contact forces P_x (top row) and P_y (bottom row) during sliding for the two-half-pass (2hp) and full-pass (fp) contact algorithms considering $\mu = 0.5$, $m = 16$ and $\epsilon = 100 E_0/L_0$. Left: overview; middle: enlargement for $n_{\bar{u}} = 20$; right: enlargement for $n_{\bar{u}} = 80$. For 2hp, P_1 denotes the force acting on the half-cylinder, while P_2 denotes the force acting on the block.

- influence of the loading step number $n_{\bar{u}}$ (Fig. 11),
- influence of the starting step for friction (Fig. 12),
- comparison between two-half-pass (2hp) and full-pass (fp) results (Fig. 13),
- influence of the FE mesh density (Fig. 14),
- influence of the penalty parameter ϵ (Fig. 15).

Fig. 11 shows the convergence of the 2hp results to the ‘exact’ solution for increasing values of $n_{\bar{u}}$. The left column figures show the contact tractions acting on $\partial\mathcal{B}_1$, the middle column shows the tractions on $\partial\mathcal{B}_2$. The blue and red curves display the raw, i.e. quadrature point, data for the normal pressure and the tangential traction according to Eq. (48).¹⁰ The corresponding black curves (dashed and solid) display the smoothed pressure and shear according to the post-processing scheme of [17]. These curves are then compared in the right column figures. In theory the contact tractions are equal for both bodies. But numerically the 2hp approach results produces differences. As seen, the agreement (w.r.t. each other and w.r.t the ‘exact’ solution) is excellent for the contact pressure.¹¹ For the tangential traction, significant differences appear. These decrease with increasing $n_{\bar{u}}$. The reason for this lies in the inaccurate determination of the initial contact point for coarse load stepping and the inaccurate determination of the trial traction that results from this. The inaccuracy therefore only affects the tangential contact traction and not the normal contact pressure.

Fig. 11 also shows that the raw data is characterized by two sets of superposed oscillations: a

¹⁰For comparison a minus sign is included for the traction on body \mathcal{B}_1 .

¹¹A significant difference appears between the raw and the post-processed data at the boundary of contact. This is caused by the smoothing property of the post-processing scheme.

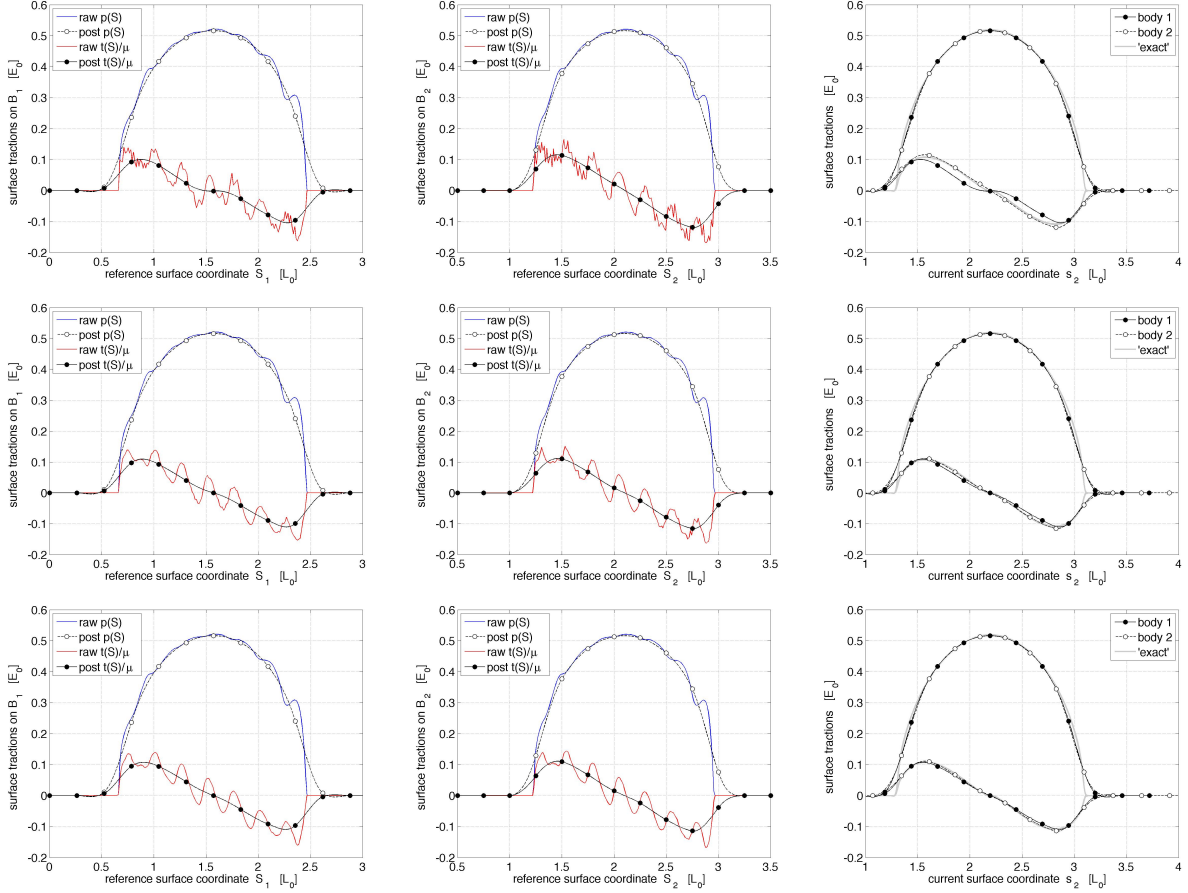


Figure 11: 2D frictional ironing; convergence with load step number $n_{\bar{u}}$: Accuracy of the contact tractions for the downward motion (at $\bar{u}_y = 2/3L_0$) for $m = 8$, $\epsilon = 100 E_0/L_0$ and $n_{\bar{u}} \in \{30, 75, 300\}$ (top to bottom). Left column: tractions on $\partial\mathcal{B}_1$; middle column: tractions on $\partial\mathcal{B}_2$; right column: post-processed tractions for both surfaces, plotted onto $\partial\mathcal{B}_2$ and compared to the ‘exact’ tractions.

fine scale oscillation that vanishes as the load step refines, and a coarse scale oscillation that is a combined effect of the penalty regularization and the coarse finite element mesh [17]. The latter oscillations decrease for mesh refinement (see Fig. 14) and increase for increasing penalty parameter (see Fig. 15).

As seen, the accurate determination of the time of initial contact is critical to the accurate determination of the tangential contact tractions. This is particularly true for the 2hp algorithm since it uses two independent sets of contact points on both surfaces. In general, there are two reasonable choices for the time of initial contact: Selecting the load step before contact was first detected, or selecting the load step after contact was first detected.¹² Consequently, the friction algorithm is then activated respectively in the first or second step after contact detection. This can have a major influence on the accuracy of the 2hp results as Fig. 12 shows. As seen, considering friction to be active from the first step on, yields much less accurate results. As can be expected, this inaccuracy decreases if $n_{\bar{u}}$ increases, as is seen in Fig. 11, where friction is active from the first detected contact step on.

Fig. 13 shows a comparison between the 2hp and the fp results. For both cases friction is

¹²The time of initial contact can also be interpolated from the velocities and positions at the two load steps. This is not considered here.

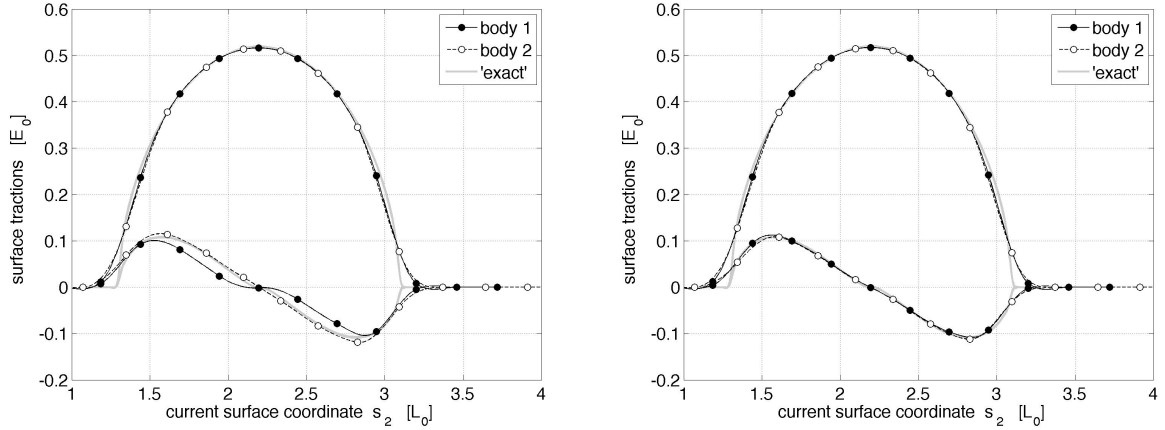


Figure 12: 2D frictional ironing: Contact tractions for the two-half-pass algorithm considering frictional contact to be active from the first (left) or second (right) step when normal contact is detected. Here $m = 8$, $n_{\bar{u}} = 20$ and $\epsilon = 100 E_0/L_0$.

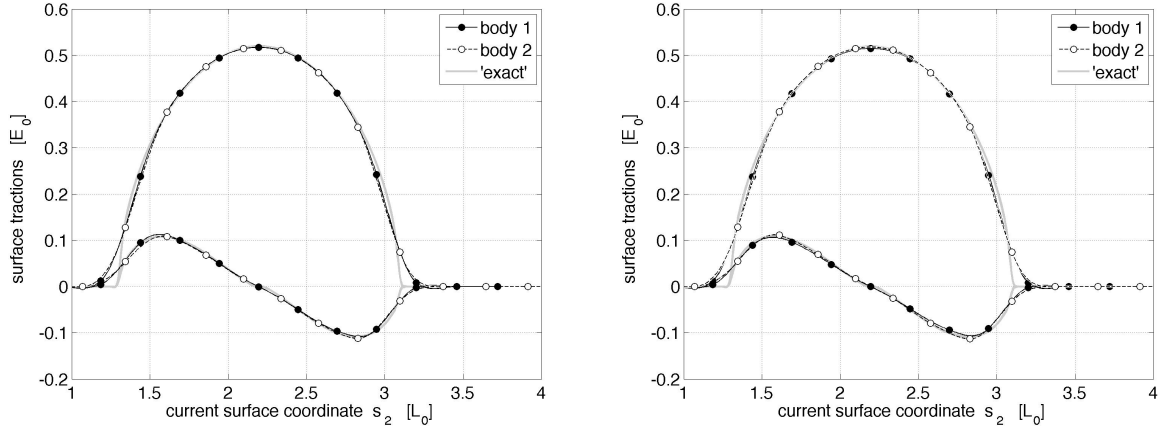


Figure 13: 2D frictional ironing: comparison of the two-half-pass algorithm (left) with the full-pass contact algorithm (right). In case of the full-pass, the two cases ‘body 1’ and ‘body 2’ refer to the chosen slave body. Here $m = 8$, $n_{\bar{u}} = 20$ and $\epsilon = 100 E_0/L_0$.

active from the second step on. The figure shows that the two traction curves from the 2hp algorithm are of comparable accuracy than the curves of the two fp variants (that are obtained by switching the slave and master designation). Thus, the 2hp difference is of the same order than the difference between the two fp variants. In terms of the CPU time, the fp is faster, since only one surface loop is required instead of two successive surface loops: For the $m = 16$ mesh, the fp with \mathcal{B}_1 as slave is about 30% faster, while the fp with \mathcal{B}_2 is about 12% faster. The 2hp, on the other hand, is more robust than the fp, especially if the fp uses the coarser surface as slave surface. In the present example, $n_{\bar{u}} = 20$ only runs for the 2hp and fp with \mathcal{B}_1 as slave. The fp with \mathcal{B}_2 as slave fails for such a coarse load step. $n_{\bar{u}} = 25$ steps were needed for this fp variant.

The following figure (Fig. 14) shows the convergence of the 2hp results to the ‘exact’ solution for increasing values of mesh parameter m . The arrangement of the data is the same as in Fig. 11 (see description above). To exclude errors coming from load stepping, a larger number of load steps is considered. Close inspection of the tangential tractions shows that even for

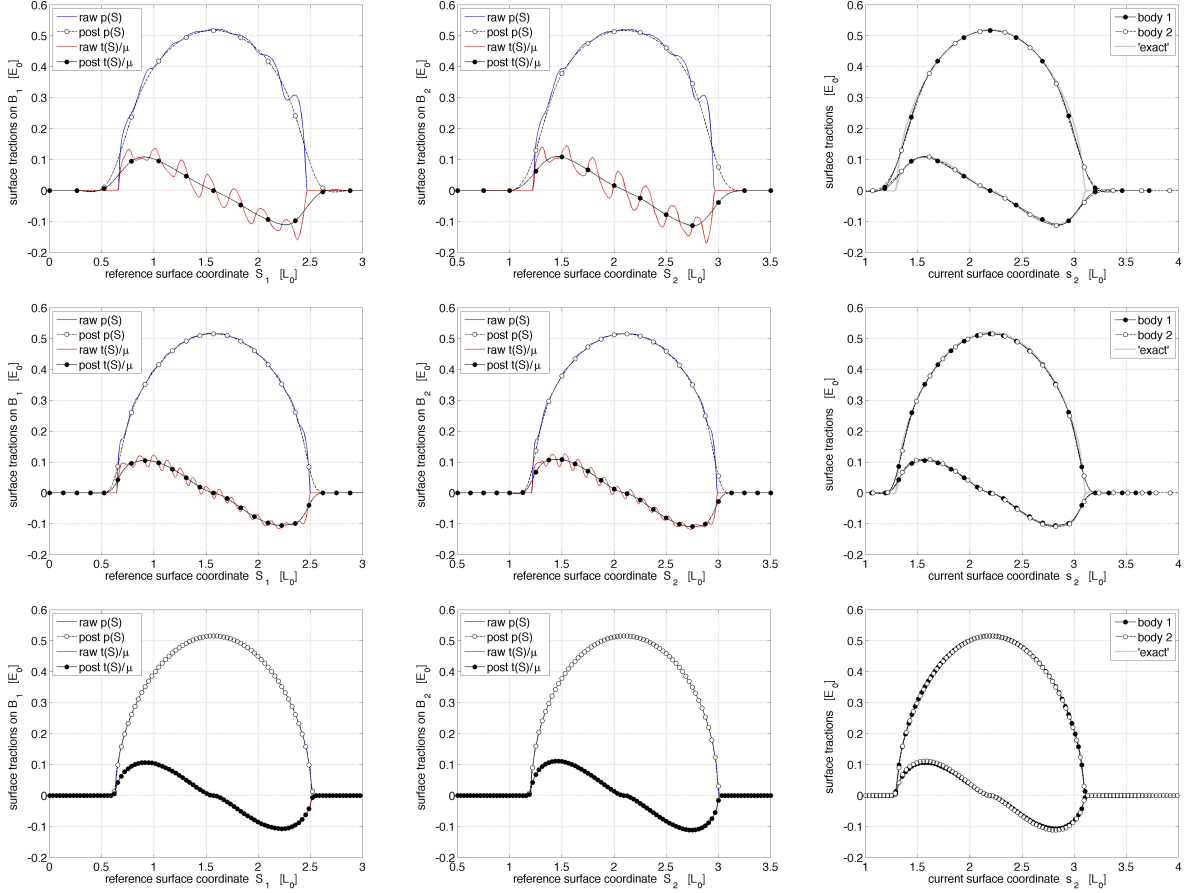


Figure 14: 2D frictional ironing; convergence with mesh density m : Accuracy of the contact tractions for the downward motion (at $\bar{u}_y = 2/3L_0$) for $m = \{8, 16, 64\}$ (top to bottom), $\epsilon = 100 E_0/L_0$ and $n_{\bar{u}} = 1200$. Left column: tractions on $\partial\mathcal{B}_1$; middle column: tractions on $\partial\mathcal{B}_2$; right column: post-processed tractions of both surfaces compared to the ‘exact’ value.

$m = 64$ differences between the two-half-pass results remain. These are caused by the penalty regularization and the resulting non-agreement of the contact surfaces. Increasing the penalty parameter therefore leads to the decrease of the remaining difference in the tangential tractions. This is shown on the right hand side of Fig. 15. The arrangement of Fig. 15 is again the same as in Figs. 11 and 14. For clarity, now an enlargement of the tangential tractions is shown. Note that the results in the bottom row corresponds to the ‘exact’ case considered in all the other figures. We also note that apart from convergence, the increase of ϵ also leads to the increase in the oscillations of the raw tractions (shown on the left and in the middle of Fig. 15), and, for very large ϵ , also an overall loss of accuracy due to ill-conditioning. This indicates that the proposed formulation becomes unstable if ϵ is increased for a fixed mesh. If the mesh density is increased along with ϵ (which it should in order to eliminate discretization errors), the formulation remains stable while converging to the exact answer. This is demonstrated by the example of Sec. 4.3. Even though the raw (= quadrature level) tractions increasingly oscillate here, the post-processed tractions converge. This is in agreement with the results in Fig. 20.

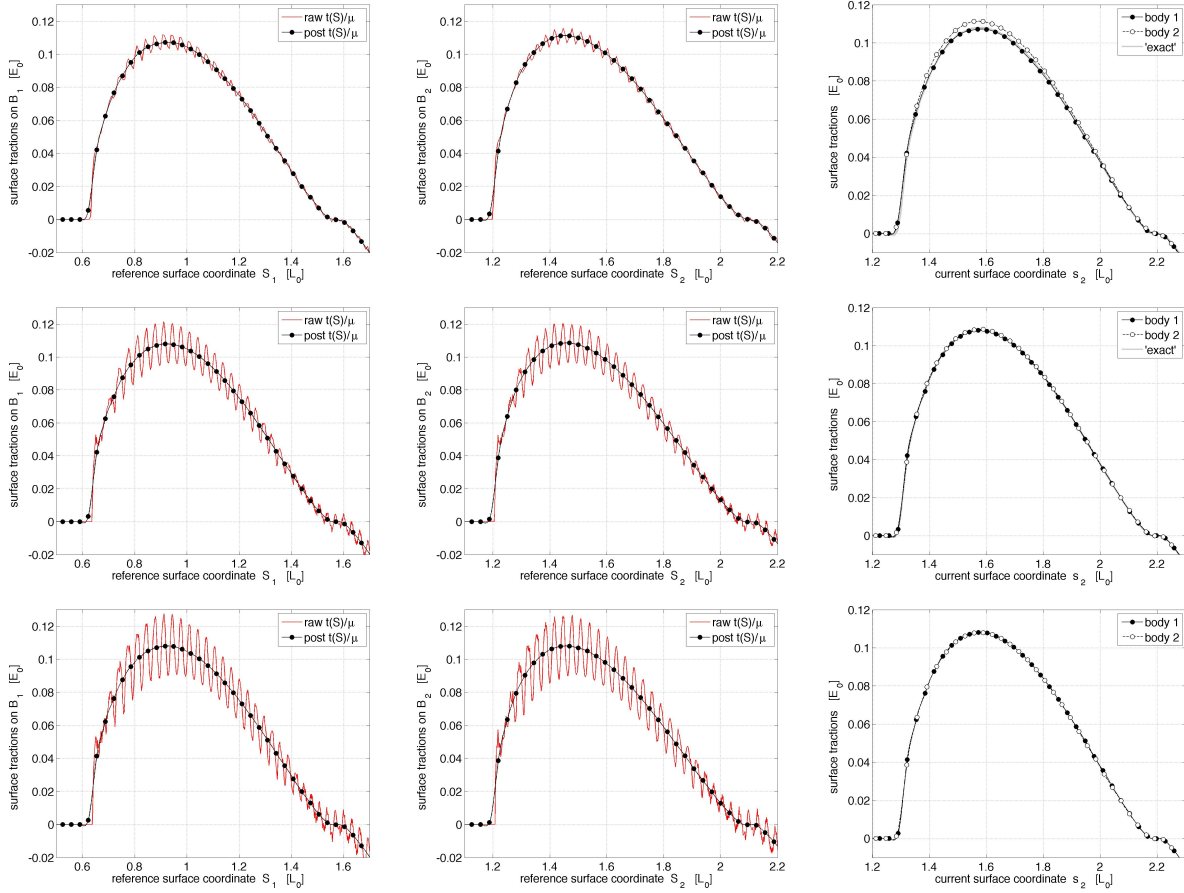


Figure 15: 2D frictional ironing; convergence with penalty ϵ : Accuracy of the tangential contact tractions for the downward motion (at $\bar{u}_y = 2/3L_0$) for $m = 64$, $\epsilon = \{100, 400, 1000\}E_0/L_0$ (top to bottom) and $n_{\bar{u}} = 1200$. Left column: tractions on $\partial\mathcal{B}_1$; middle column: tractions on $\partial\mathcal{B}_2$; right column: post-processed tractions of both surfaces compared to the ‘exact’ value.

4.2.4 Contact tractions during sliding

We now take a look at the contact tractions during the sliding motion. In the previous case (during the downward motion), sliding did not occur. It therefore remains to be seen that the 2hp algorithm correctly captures the contact tractions for sliding and for the stick/slip transition. According to the considered sliding law (4), the tangential traction is proportional to the normal pressure. Therefore, since the normal pressure matches so well for the two-half-passes, it can be expected that sliding should also work well for the 2hp algorithm. This is confirmed by the results shown in Fig. 16. The arrangement is again the same as in previous figures (e.g. see Fig. 11). The considered state is one where the contact surface is partially sticking and partially sliding. The sliding regime is the portion where $t = p\mu$. This occurs towards the boundary of the contact surface. Otherwise, towards the middle, the surfaces are still sticking. The results of Fig. 16 show an excellent agreement of the 2hp tractions, both w.r.t. each other and w.r.t the ‘exact’ solution. This is in spite of the fact that a very coarse load step is used ($n_{\bar{u}} = 16$). The reason for this is that the determination of initial contact, as noted in Sec. 4.2.3 is only crucial for sticking and not for sliding. Here, now, sticking occurs only in the middle of the contact surface where all surface points are already in contact. As a result, the excellent agreement of the 2hp tractions with the ‘exact’ solution is maintained throughout the sliding phase and the preceding stick/slip transition as is shown in Fig. 17. Inaccuracies

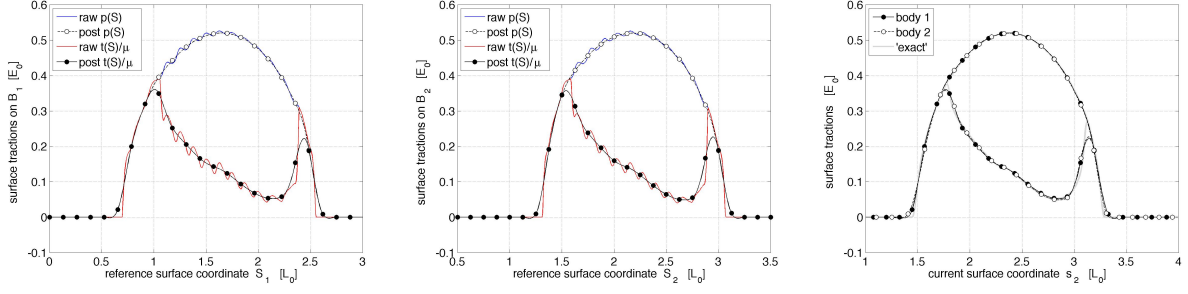


Figure 16: 2D frictional ironing: Accuracy of the contact tractions during the sliding motion (at $\bar{u}_x = L_0/4$) for $m = 16$, $\epsilon = 100 E_0/L_0$, $n_{\bar{u}} = 16$. Left: tractions on ∂B_1 ; middle: tractions on ∂B_2 ; right: post-processed traction of both surfaces compared to ‘exact’ value.

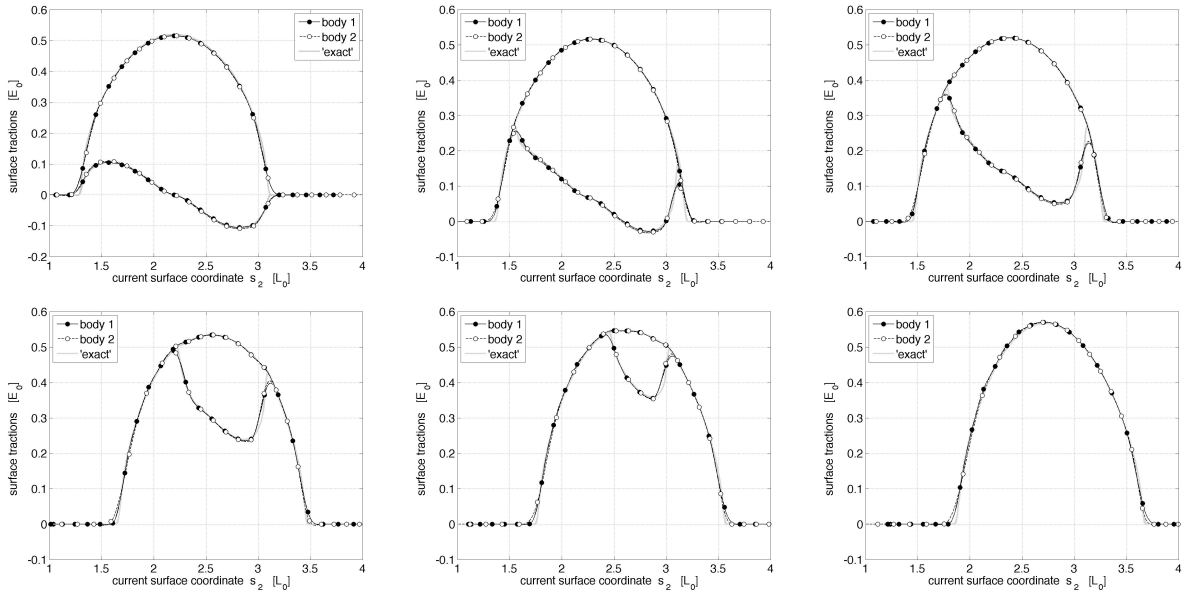


Figure 17: 2D frictional ironing: Contact tractions during the sliding motion at $\bar{u}_x = \{0, 1, 2, 4, 5, 6\} \times L_0/8$ (top left to bottom right) for $m = 16$, $\epsilon = 100 E_0/L_0$ and $n_{\bar{u}} = 16$.

remain at the boundary of contact and the boundary between stick and slip. These are due to the smoothing property of the post-processing scheme. For the computational results of Figs. 16 and 17, the starting configuration from the preceding downward pressing was obtained with a very small load step ($n_{\bar{u}}$) to eliminate errors there. It has been confirmed that also during the sliding phase the agreement between the tractions of the 2hp algorithm and fp algorithms (for both variants) is as good as in the downward motion (Fig. 13).

From the traction analysis of this section and the preceding section, we can conclude that also in the case of frictional sticking and sliding contact, just like in the case of frictionless contact [1], the 2hp properly captures the traction continuity at the contact interface. This is consistent with the theoretical proof available for the continuum [1].

4.3 Sliding contact between two rings

The third example considers sliding contact between two concentric rings. The example is used to study the stability and convergence behavior for the proposed two-half-pass (2hp) friction algorithm. Two rings, \mathcal{B}_1 and \mathcal{B}_2 , with initial radii $R_1 \in [1, 2]L_0$ and $R_2 \in [2, 3]L_0$ are considered as shown in Fig. 18a. The two rings are both discretized by $m \times 12m$ finite elements, considering various values for m . Hermite-enriched contact elements Q1CH are used along the contact interface at $R = 2L_0$. The rings are modeled by constitutive model (47), considering

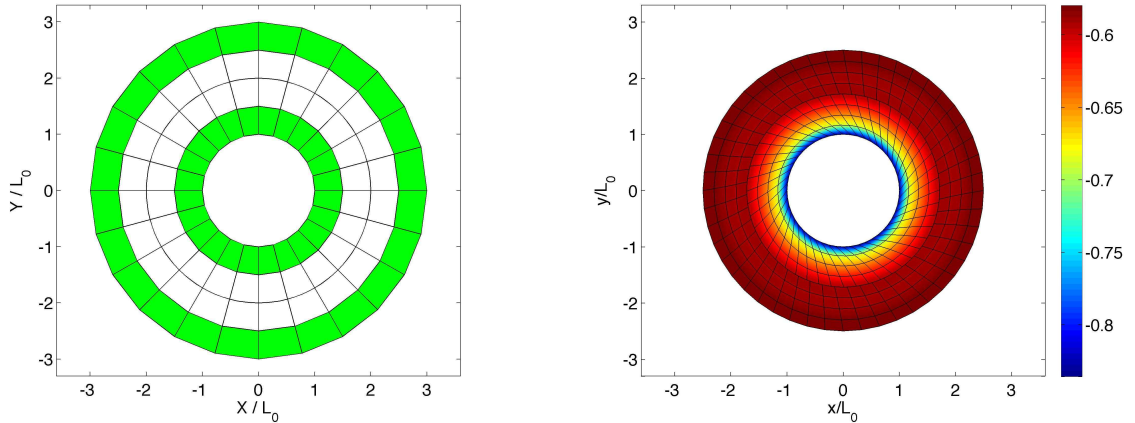


Figure 18: Sliding contact between two rings: left: undeformed initial configuration (here for 4×24 elements ($m = 2$), standard Q1 elements in green, Q1CH elements in white); right: Deformed configuration (here for 8×48 elements ($m = 4$)) for the radial displacement $\bar{u}_r = L_0/2$ and rotation angle 30° ; the coloring shows the radial stress component σ_{rr} .

$E = E_0$ and $\nu = 0.3$. Sliding is modeled by Coulomb's law (4), using $\mu = 0.2$. The inner boundary, at $R = L_0$, is considered fixed. On the outer boundary, at $R = 3L_0$, an inward radial displacement of $\bar{u}_r = L_0/2$ is applied, during which, due to rotational symmetry, no sliding occurs. Then a counter-clockwise rotation is applied to the outer boundary, which leads to the deformed configuration shown in Fig. 18b. Sliding occurs beyond 28.535° , when the shear traction on the interface reaches μ -times the interface pressure. This result can be obtained without using any contact algorithm – simply using a connected mesh. In this manner a highly accurate reference solution was obtained (using $m = 128$) that is independent of the contact algorithm. Fig. 19 shows the convergence behavior of the 2hp friction algorithm to the reference solution by looking at the errors in the interface radius and the contact pressure

$$\text{err}(r) = \left| \frac{r_{\text{ref}} - r(\epsilon, m)}{r_{\text{ref}}} \right|, \quad \text{err}(p) = \left| \frac{p_{\text{ref}} - p(\epsilon, m)}{p_{\text{ref}}} \right| \quad (49)$$

for various values of the penalty parameter $\epsilon = \epsilon_n = \epsilon_t$ and the mesh parameter m . Here $r(\epsilon, m)$ and $p(\epsilon, m)$ are averaged over the sliding path of $30^\circ/m$ (corresponding to the sliding of one contact element) considering 15 load increments.¹³ The figure shows that, for fixed m , the convergence stagnates for high values of ϵ , since an increase of ϵ only removes the penetration error but not the discretization error associated with m .¹⁴ Once the curve stagnates,

¹³Here, the pressure is determined from the normal component of the nodal contact forces. Due to rotational symmetry, it is, like r , equal for all nodes.

¹⁴During convergence, r_o and p_o approach r_{ref} and p_{ref} from below, while r_i and $-p_i$ first approach r_{ref} and $-p_{\text{ref}}$ from above, pass r_{ref} and $-p_{\text{ref}}$ and then approach r_{ref} and $-p_{\text{ref}}$ from below. This leads to the dip in the convergence curves for r_i and p_i .

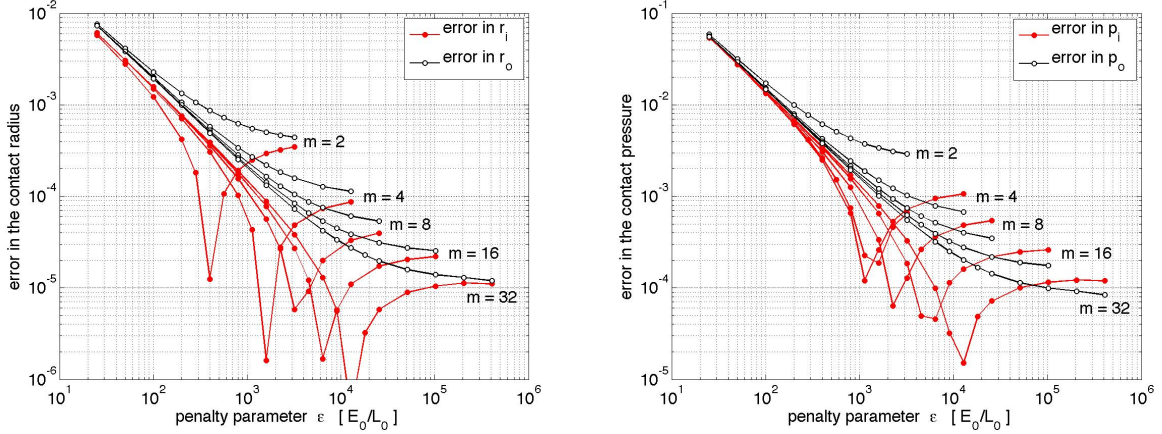


Figure 19: Sliding contact between two rings: Convergence behavior of the two half-pass-algorithm examining the interface radius (left) and the contact pressure (right); r_i , r_o , p_i and p_o correspond to the values of the inner and outer contact surfaces.

increasing ϵ further is not useful, but rather counter-productive, since an increase in ϵ leads to ill-conditioning. This is shown in Fig. 20.¹⁵ The figure demonstrates that ill-conditioning does

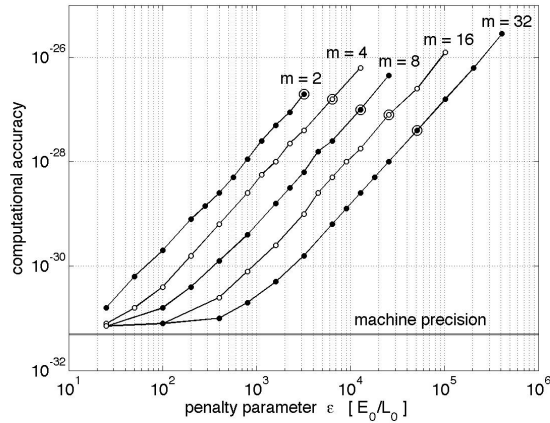


Figure 20: Sliding contact between two rings: Computational accuracy of the Newton-Raphson iteration in the energy norm for various penalty and mesh parameters. The denser the mesh (increasing m), the higher ϵ can be taken to obtain the same accuracy; an example is the sequence marked by ‘o’ that is then used in Fig. 21.

not affect accuracy significantly since no more than 6 digits are lost in the energy norm (out of almost 32). For large ϵ , the computation may altogether fail, due to a loss of convergence in the Newton-Raphson iteration. This occurs beyond the values shown in Fig. 20. This failure can be attributed to the tendency of over-constraining in the 2hp algorithm that eventually leads to an unstable setup.¹⁶ The computational failure is also related to the number of loading steps during sliding. Lowering the step size will allow using larger ϵ without failure. As is seen

¹⁵The data shown here was averaged over the various iteration steps during sliding, determining the exponent of the computational accuracy only up to ± 0.1 , which explains the wiggles in the curves.

¹⁶Here, 10 Gaussian quadrature points are used for each surface element on the contact surface. Since all these points remain actively in contact, the contact constraint is thus enforced at 20 locations for each pair of neighboring Q1CH elements, which use cubic interpolation.

from Fig. 19, the failure due to over-constraining only becomes an issue once the convergence behavior anyway stagnates due to fixed m . The problem of stagnation and over-constraining is avoided if the number of elements and the step size are increased along with the penalty parameter. This is shown in Fig. 21, where ϵ and the step size are increased linearly with m . For such an increase the computation accuracy even improves, as the ‘o’ in Fig. 20 show. This

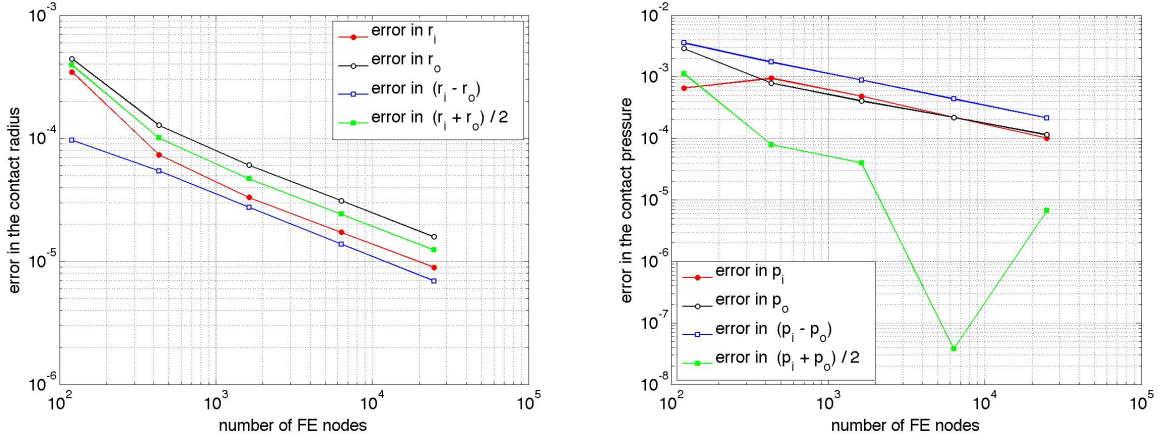


Figure 21: Sliding contact between two rings: Convergence behavior of the interface radius (left) and the contact pressure (right) for $m = \{2, 4, 8, 16, 32\}$ considering $\epsilon = 1600 m E_0/L_0$ and a stepsize of $30^\circ/m$.

shows that the 2hp algorithm can be used to compute frictional contact robustly and accurately, converging without problems to the exact solution.¹⁷ Fig. 21 also shows that the 2hp errors $(r_i - r_o)$ and $(p_i - p_o)$ and averages $(r_i + r_o)/2$ and $(p_i + p_o)/2$ converge at the same rate and are of comparable accuracy than r_i , r_o , p_i and p_o . We can thus conclude that the 2hp error is of the same magnitude as the overall discretization error.

4.4 Twisting contact between a hemisphere and a block

The next example considers 3D frictional twisting contact between a hemisphere and a block. Fig. 22 shows the considered problem setup. A thick, hollow half-sphere (\mathcal{B}_1) is pressed into a solid block (\mathcal{B}_2) and then twisted as shown. The dimensions of the block are $L_0 \times L_0 \times L_0$; the outer radius of the hollow sphere is L_0 , the inner radius is $2/3 L_0$. Initially a downward motion of $\bar{u} = L_0$ is applied to the sphere and then maintained during twisting. Both bodies are modeled as Neo-Hookean (47), where the Young’s modulus of the sphere is taken five times larger than that of the block ($E_1 = 5E_0$, $E_2 = E_0$). Poisson’s ratio is taken as $\nu = 0.3$ for both bodies. Friction leads to large shear deformation of block and sphere. Coulomb friction (4) is considered with $\mu = 0.5$. For simplicity, the downward motion is modeled frictionless here. The penalty parameters are chosen as $\epsilon_n = \epsilon_t = \epsilon = 100 E_0/L_0$. The two contact surfaces are modeled with NURBS enriched contact elements [25], while the rest of the bodies is modeled with linear elements. 10×10 Gaussian quadrature points are used for the evaluation of the contact integrals. The meshes contain $n_{el1} = 4 \cdot 11^2$ and $n_{el1} = 8^3$ volume elements and $n_{cell} = 11^2$ and $n_{cell} = 8^2$ surface elements on the contact surface.

¹⁷Convergence to the exact answer implies the disappearance of the mesh discretization error (convergence in h) and the constraint-enforcement error (convergence in ϵ). The stability of contact algorithms is often only assessed from the latter. In that sense our approach appears unstable. But it is stable when simultaneous convergence (here with $\epsilon \sim h^{-1}$) is examined. This is in agreement with mathematical convergence theory [31].

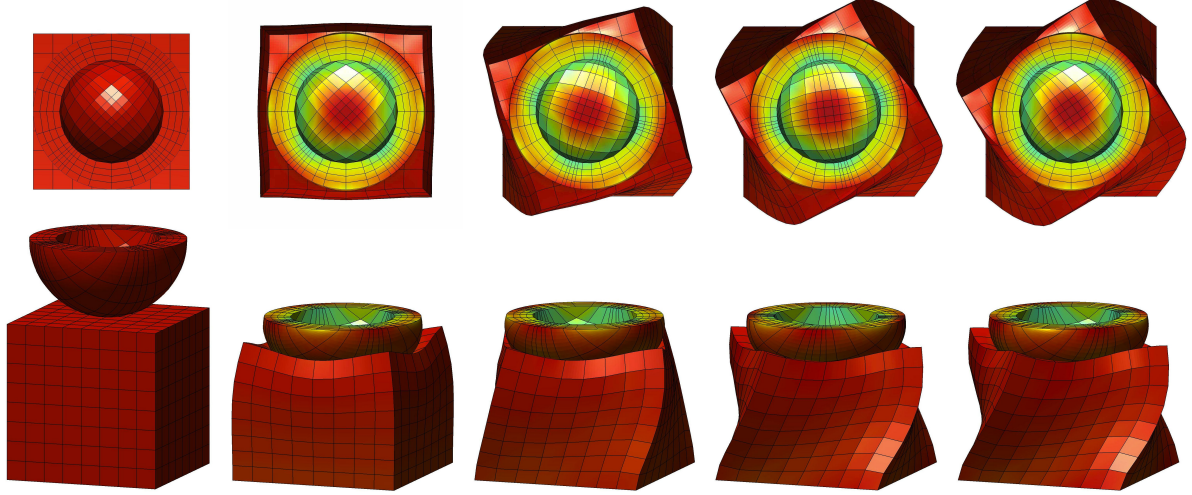


Figure 22: Frictional twisting: Undeformed configuration (far left); deformation and stress $I_1 = \text{tr } \boldsymbol{\sigma}$ (normalized by E_0) for twisting angles 0, 30, 60 and 180 degrees (left to right). The colorscale is the same as in Fig. 23.

Fig. 23 shows the stress fields I_1 and σ_{zz} (vertical normal stress component) inside the block and sphere at a twisting angle of 90 degrees. The view shows the large deformations inside the

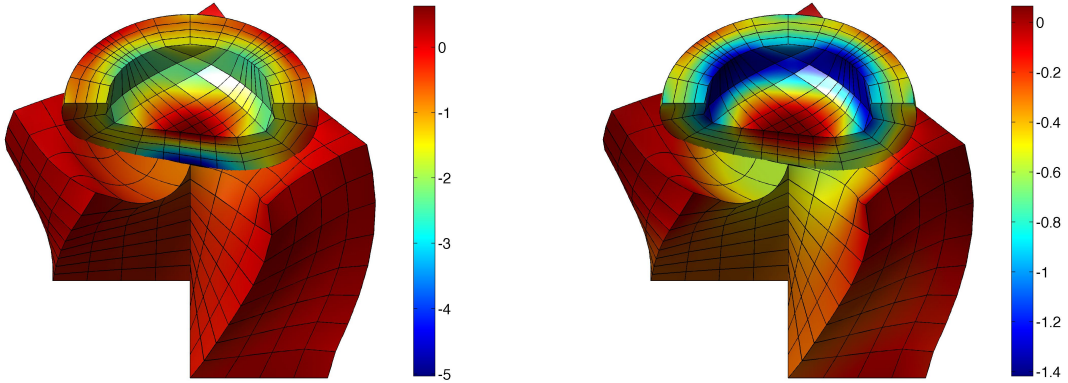


Figure 23: Frictional twisting: Deformation and stresses I_1 (left) and σ_{zz} (right), both normalized by E_0 , at a twisting angle of 90 degrees. Parts of the block and sphere are removed for this display.

two bodies. I_1 is particularly large inside the sphere, due to its contact induced bending. Further, Fig. 24 shows the global contact force P_z and torque M_z during twisting. Sliding starts to occur on the boundary of the contact surface and then progresses inward until the entire contact surface is in sliding. This occurs from an angle of 118 degrees on. Since the shear tractions at the center of the contact surface hardly contribute to the twisting torque M_z , the M_z curve appears to flatten out much earlier. The enlargements in Fig. 24 show that for all methods (2hp, both fp variants) both P_z and M_z vary strongly during sliding. This is an error introduced by the discretization, as in theory P_z and M_z should be constant during sliding, since there is no deformation change of block and sphere (only a rigid rotation is superposed onto the existing deformation). The discretization error can be assessed from the comparison with the refined 2hp solution that is included in Fig. 24 for reference (considering $n_{\text{el1}} = 6 \cdot 19^2$ and $n_{\text{el1}} = 16^3$ elements, and $\epsilon = 750E_0/L_0$). The discretization error is about as large as the

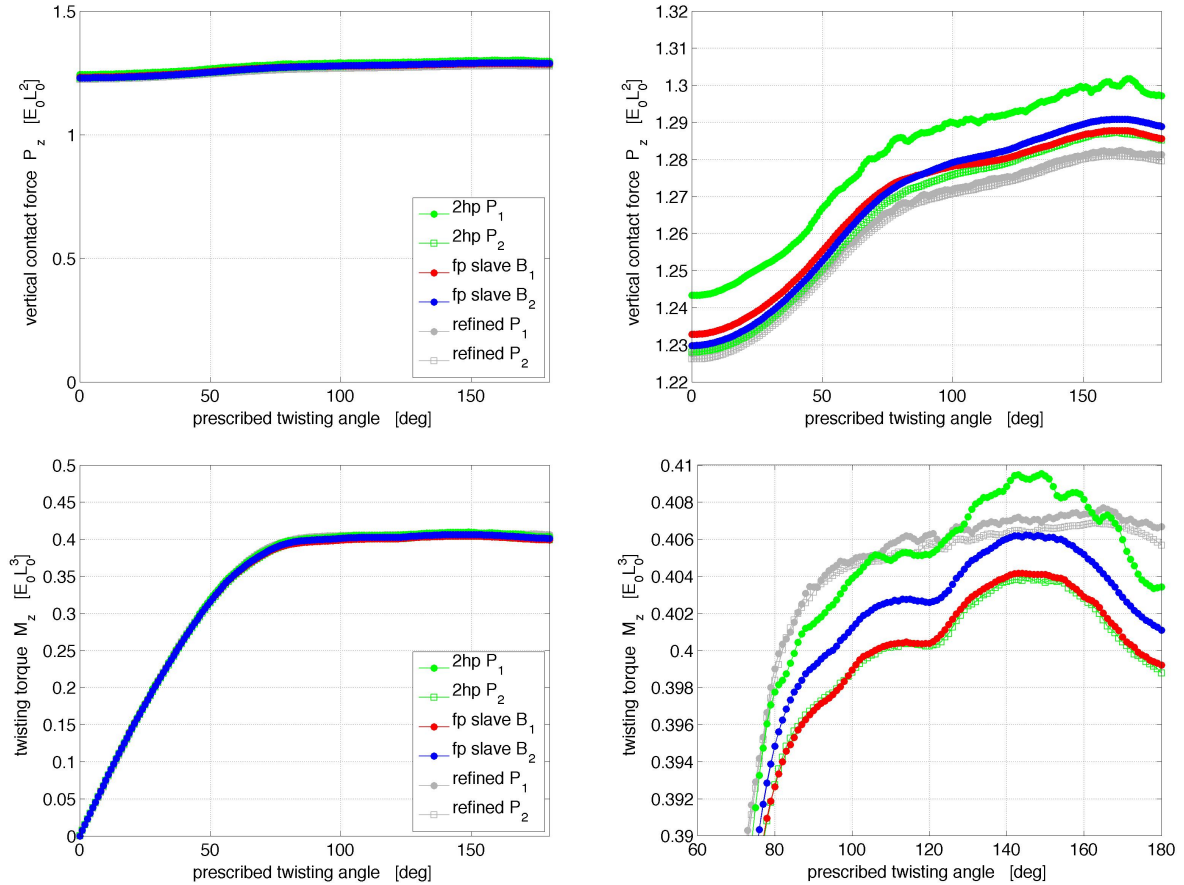


Figure 24: 3D twisting contact: Net contact force P_z and contact torque M_z according to the two-half-pass (2hp) and full-pass (fp) contact algorithms. Left: overview; right: enlargement. The comparison with the refined solution shows that both algorithms lead to discretization errors of the same order.

difference between the 2hp results. In other words, we again find that the error in the 2hp algorithm is of the same order than the discretization error that is present anyway.

Finally, Fig. 25 displays the contact tractions during sliding (at a twisting angle of 180 degrees). These tractions are taken from the 2hp result, employing the post-processing algorithm of [17]. As seen, a nice match is found between the traction fields on the two surfaces. This once more demonstrates that the 2hp algorithm captures the traction continuity across the contact interface, even though this continuity is not imposed explicitly within the algorithm.

5 Conclusion

This paper presents the extension of the two-half-pass contact algorithm of [1] to 3D friction. This algorithm is essentially a reduction of the full-pass contact algorithm and its implementation is fairly straight forward if a working full-pass algorithm is available. The two-half-pass algorithm does not explicitly enforce traction continuity at the contact interface. This distinguishes it from past approaches. The consequence is the appearance of a small continuity error, which does not compromise the overall accuracy since it is of the same order as the finite element discretization error. This was already shown for frictionless contact in [1]. Here we

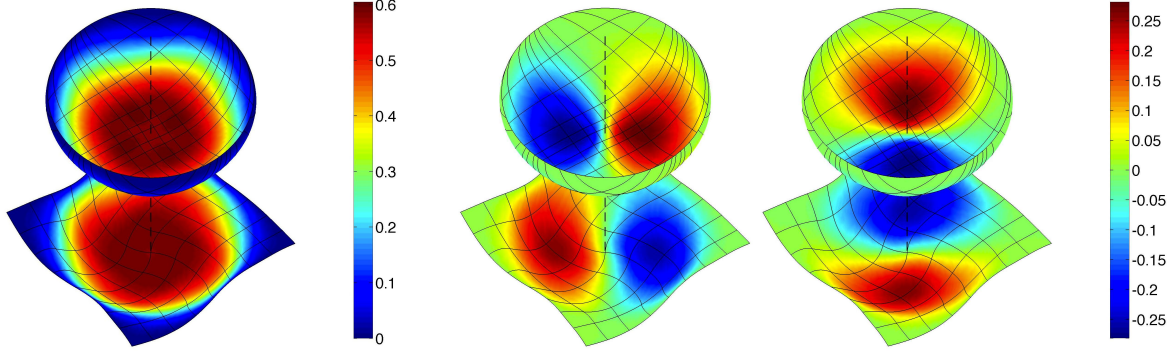


Figure 25: 3D twisting contact: Contact pressure p (left) and tangential contact traction components $t_x = \mathbf{t}_t \cdot \mathbf{e}_x$ (middle) and $t_y = \mathbf{t}_t \cdot \mathbf{e}_y$ (right), both normalized by E_0 , acting on the deformed surfaces $\partial\mathcal{B}_1$ and $\partial\mathcal{B}_2$. In this view \mathbf{e}_x appears to point downward, while \mathbf{e}_y points to the right. For clarity the two surfaces have been moved apart. The dashed line shows the twisting axis.

have now shown this also to be true for frictional contact using a set of challenging 2D and 3D examples. Among those are a detailed analysis of the influence of the model parameters and a convergence analysis that demonstrates the maintained stability of the proposed formulation as $\epsilon \rightarrow \infty$. Included is also a simple test case that illustrates the advantage of the two-half-pass approach over the full-pass approach, and which is also useful to validate the implementation. In this paper, friction is described by a new sticking formulation based on a penalty regularization and a predictor-corrector algorithm. As shown, the new formulation becomes equal to existing formulations in the continuum limit. All contact computations presented here employ C^1 -continuous contact surfaces based on Hermite interpolation in 2D and NURBS interpolation in 3D. In summary, the proposed new approach provides an unbiased algorithm for frictional contact that is robust and highly accurate. The current approach is based on a non-mortar contact formulation. The extension to mortar methods will be considered in future work.

Acknowledgements

The authors are grateful for the support of the European Research Council (ERC starting researcher grant ‘INTERFACES’, no. 279439), the German Research Foundation (grants SA1822/5-1 and GSC111) and the Northrhine-Westphalian Academy of the Sciences and Arts. The authors also thank Callum Corbett for his help in implementing 3D contact.

A Equivalency of friction formulations

Here we show the equivalency between the proposed trial traction formulation (25) and the formulations of Laursen (19) and Wriggers (21) as $\Delta t \rightarrow 0$ and $\epsilon_t \rightarrow \infty$. For small Δt , the tangent planes at $\boldsymbol{\xi}_p^n$ and $\boldsymbol{\xi}_p^{n+1}$ are approximately equal so that (25) turns into

$$\mathbf{t}_{t_{n+1}}^{\text{trial}} \approx \mathbf{t}_{t_n}^{\text{up}} + \epsilon_t (\boldsymbol{\xi}_{p_{n+1}}^\alpha - \boldsymbol{\xi}_{p_n}^\alpha) \mathbf{a}_{\alpha_{n+1}}^p, \quad (50)$$

where $\mathbf{a}_{\alpha_{n+1}}^p$ are the basis vectors of the common tangent plane. For large ϵ_t , the distance $\Delta \boldsymbol{\xi}_e^n = \boldsymbol{\xi}_p^n - \boldsymbol{\xi}_s^n$ is small and thus the tangent planes at $\boldsymbol{\xi}_s^n$ and $\boldsymbol{\xi}_p^n$ are also approximately equal. For $\mathbf{t}_{t_n}^{\text{up}}$, defined in Eq. (24), we thus find

$$\mathbf{t}_{t_n}^{\text{up}} \approx \epsilon_t (\boldsymbol{\xi}_{p_n}^\alpha - \boldsymbol{\xi}_{s_n}^\alpha) \mathbf{a}_{\alpha_{n+1}}^p \approx \epsilon_t (\boldsymbol{\xi}_{p_n}^\alpha - \boldsymbol{\xi}_{s_n}^\alpha) \mathbf{a}_{\alpha_n}^p = \mathbf{t}_t^n. \quad (51)$$

Here $t_{tn}^\alpha = \epsilon_t(\xi_{pn}^\alpha - \xi_{sn}^\alpha)$ are the contra-variant components of \mathbf{t}_t^n . Inserting Eq. (51) into Eq. (50) reproduces either expression (21) or yields

$$\mathbf{t}_{tn+1}^{\text{trial}} = \left[t_{tn}^\alpha + \epsilon_t(\xi_{pn+1}^\alpha - \xi_{pn}^\alpha) \right] \mathbf{a}_{\alpha n+1}^p, \quad (52)$$

which is equivalent to expression (19).

B Tangent matrices

Here we provide the tangent matrices for the two-half-pass algorithm. These are contained in the tangent matrices of the full-pass algorithm, which we also report here. In the latter case, the contact force vectors, acting on the nodes of elements Γ_k^e and Γ_ℓ^e are given by

$$\begin{aligned} \mathbf{f}_{ck}^e &= - \int_{\Gamma_k^e} \mathbf{N}_k^T \mathbf{t}_k \, da_k = - \int_{\Gamma_{0k}^e} \mathbf{N}_k^T \mathbf{t}_k J_k \, dA_k, \\ \mathbf{f}_{c\ell}^e &= \int_{\Gamma_\ell^e} \mathbf{N}_\ell^T \mathbf{t}_k \, da_k = \int_{\Gamma_{0k}^e} \mathbf{N}_\ell^T \mathbf{t}_k J_k \, dA_k. \end{aligned} \quad (53)$$

Note that $\mathbf{N}_k(\boldsymbol{\xi})$ is evaluated at the point $\mathbf{x}_k = \mathbf{x}_k(\boldsymbol{\xi})$ on surface $\partial\mathcal{B}_k$, which is integrated over, while $\mathbf{N}_\ell(\boldsymbol{\xi})$ is evaluated at the projection point $\mathbf{x}_p = \mathbf{x}_\ell(\boldsymbol{\xi}_p)$ on surface $\partial\mathcal{B}_\ell$, which depends on \mathbf{x}_k , i.e. $\mathbf{x}_p = \mathbf{x}_p(\mathbf{x}_k)$.

The forces \mathbf{f}_{ck}^e and $\mathbf{f}_{c\ell}^e$ depend on the deformation (or displacement) of element $\Gamma_k^e \subset \partial\mathcal{B}_k^h$ – the element of integration – and element $\Gamma_\ell^e \subset \partial\mathcal{B}_\ell^h$ – the element on the neighboring surface where the projection point lies. It is noted that in general, for non-conforming meshes, several elements Γ_ℓ^e are affected by each Γ_k^e . The dependency is expressed as $\mathbf{f}_{ck}^e = \mathbf{f}_{ck}^e(\mathbf{u}_k^e, \mathbf{u}_\ell^e)$ and $\mathbf{f}_{c\ell}^e = \mathbf{f}_{c\ell}^e(\mathbf{u}_k^e, \mathbf{u}_\ell^e)$ where \mathbf{u}_k^e denotes the displacement vector of Γ_k^e and where \mathbf{u}_ℓ^e denotes the displacement vector of all the affected elements Γ_ℓ^e .

The linearization of \mathbf{f}_{ck}^e at $\{\mathbf{u}_k^e, \mathbf{u}_\ell^e\}$ in the direction $\{\Delta\mathbf{u}_k^e, \Delta\mathbf{u}_\ell^e\}$ yields

$$\begin{aligned} \mathbf{f}_{ck}^e(\mathbf{u}_k^e + \Delta\mathbf{u}_k^e, \mathbf{u}_\ell^e + \Delta\mathbf{u}_\ell^e) &\approx \mathbf{f}_{ck}^e(\mathbf{u}_k^e, \mathbf{u}_\ell^e) + \Delta\mathbf{f}_{ck}^e(\mathbf{u}_k^e, \mathbf{u}_\ell^e), \\ \mathbf{f}_{c\ell}^e(\mathbf{u}_k^e + \Delta\mathbf{u}_k^e, \mathbf{u}_\ell^e + \Delta\mathbf{u}_\ell^e) &\approx \mathbf{f}_{c\ell}^e(\mathbf{u}_k^e, \mathbf{u}_\ell^e) + \Delta\mathbf{f}_{c\ell}^e(\mathbf{u}_k^e, \mathbf{u}_\ell^e), \end{aligned} \quad (54)$$

with

$$\begin{aligned} \Delta\mathbf{f}_{ck}^e &= - \int_{\Gamma_{0k}^e} \mathbf{N}_k^T \Delta\mathbf{t}_k J_k \, dA_k - \int_{\Gamma_{0k}^e} \mathbf{N}_k^T \mathbf{t}_k \Delta J_k \, dA_k, \\ \Delta\mathbf{f}_{c\ell}^e &= \int_{\Gamma_{0k}^e} \Delta\mathbf{N}_\ell^T \mathbf{t}_k J_k \, dA_k + \int_{\Gamma_{0k}^e} \mathbf{N}_\ell^T \Delta\mathbf{t}_k J_k \, dA_k + \int_{\Gamma_{0k}^e} \mathbf{N}_\ell^T \mathbf{t}_k \Delta J_k \, dA_k, \end{aligned} \quad (55)$$

according to Eq. (53). Array \mathbf{N}_ℓ contributes to the linearization since it is evaluated at the coordinate of the projection point $\boldsymbol{\xi}_p$. This contribution, and the rest of Eq. (55.2), are not needed for the two-half-pass formulation. For the full-pass, where $\Delta\mathbf{N}_\ell$ is needed, we find

$$\Delta\mathbf{N}_\ell = \mathbf{N}_{\ell,\alpha} \Delta\xi_p^\alpha, \quad (56)$$

with

$$\Delta\xi_p^\alpha = \frac{\partial\xi_p^\alpha}{\partial\mathbf{u}_k^e} \Delta\mathbf{u}_k^e + \frac{\partial\xi_p^\alpha}{\partial\mathbf{u}_\ell^e} \Delta\mathbf{u}_\ell^e. \quad (57)$$

Here, as in all other equations, summation is implied on repeated Greek indices. In [1], Appendix B, we have shown that

$$\begin{aligned} \frac{\partial\xi_p^\alpha}{\partial\mathbf{u}_k^e} &= c_p^{\alpha\beta} \mathbf{a}_\beta^p \mathbf{N}_k, \\ \frac{\partial\xi_p^\alpha}{\partial\mathbf{u}_\ell^e} &= -c_p^{\alpha\beta} (\mathbf{a}_\beta^p \mathbf{N}_\ell - g_n \mathbf{n}_p \mathbf{N}_{\ell,\beta}), \end{aligned} \quad (58)$$

where $c_p^{\alpha\beta}$ are the components of the matrix

$$[c_p^{\alpha\beta}] = [a_{\alpha\beta}^p - g_n b_{\alpha\beta}^p]^{-1}, \quad (59)$$

where

$$\begin{aligned} a_{\alpha\beta}^p &:= \mathbf{a}_\alpha^p \cdot \mathbf{a}_\beta^p, \\ b_{\alpha\beta}^p &:= \mathbf{n}_p \cdot \mathbf{a}_{\alpha,\beta}^p, \end{aligned} \quad (60)$$

are the co-variant components of the metric tensor and the curvature tensor at $\mathbf{x}_p \in \partial\mathcal{B}_\ell$. For the change of the contact traction \mathbf{t}_k we have

$$\Delta \mathbf{t}_k = \frac{\partial \mathbf{t}_k}{\partial \mathbf{u}_k^e} \Delta \mathbf{u}_k^e + \frac{\partial \mathbf{t}_k}{\partial \mathbf{u}_\ell^e} \Delta \mathbf{u}_\ell^e, \quad (61)$$

which is further specified in the subsections below. The last contribution, the change in J_k , is

$$\Delta J_k = J_k \mathbf{a}_k^\alpha \cdot \mathbf{N}_{k,\alpha} \Delta \mathbf{u}_k^e, \quad (62)$$

see [1], appendix D, and [32]. With the above equations we can rewrite (55) as

$$\begin{aligned} \Delta \mathbf{f}_{ck}^e &= \mathbf{k}_{ckk}^e \Delta \mathbf{u}_k^e + \mathbf{k}_{ck\ell}^e \Delta \mathbf{u}_\ell^e, \\ \Delta \mathbf{f}_{c\ell}^e &= \mathbf{k}_{c\ell k}^e \Delta \mathbf{u}_k^e + \mathbf{k}_{c\ell\ell}^e \Delta \mathbf{u}_\ell^e, \end{aligned} \quad (63)$$

where we have introduced the tangent matrices

$$\begin{aligned} \mathbf{k}_{ckk}^e &= - \int_{\Gamma_k^e} \mathbf{N}_k^T \frac{\partial \mathbf{t}_k}{\partial \mathbf{u}_k^e} da_k - \int_{\Gamma_k^e} \mathbf{N}_k^T \mathbf{t}_k \otimes \mathbf{a}_k^\alpha \mathbf{N}_{k,\alpha} da_k, \\ \mathbf{k}_{ck\ell}^e &= - \int_{\Gamma_k^e} \mathbf{N}_k^T \frac{\partial \mathbf{t}_k}{\partial \mathbf{u}_\ell^e} da_k, \\ \mathbf{k}_{c\ell k}^e &= \int_{\Gamma_k^e} \mathbf{N}_{\ell,\alpha}^T \mathbf{t}_k \otimes \frac{\partial \xi_p^\alpha}{\partial \mathbf{u}_k^e} da_k + \int_{\Gamma_k^e} \mathbf{N}_\ell^T \frac{\partial \mathbf{t}_k}{\partial \mathbf{u}_k^e} da_k + \int_{\Gamma_k^e} \mathbf{N}_\ell^T \mathbf{t}_k \otimes \mathbf{a}_k^\alpha \mathbf{N}_{k,\alpha} da_k, \\ \mathbf{k}_{c\ell\ell}^e &= \int_{\Gamma_k^e} \mathbf{N}_{\ell,\alpha}^T \mathbf{t}_k \otimes \frac{\partial \xi_p^\alpha}{\partial \mathbf{u}_\ell^e} da_k + \int_{\Gamma_k^e} \mathbf{N}_\ell^T \frac{\partial \mathbf{t}_k}{\partial \mathbf{u}_\ell^e} da_k. \end{aligned} \quad (64)$$

We again note that in general, different elements Γ_ℓ^e of surface $\partial\mathcal{B}_\ell^h$ are affected within the integration.

The contact traction is composed of a normal and tangential contribution, which according to the signs introduced in Sec. 2 combine as $\mathbf{t}_k := \mathbf{t}_n - \mathbf{t}_t$, thus

$$\frac{\partial \mathbf{t}_k}{\partial \mathbf{u}_\bullet^e} = \frac{\partial \mathbf{t}_n}{\partial \mathbf{u}_\bullet^e} - \frac{\partial \mathbf{t}_t}{\partial \mathbf{u}_\bullet^e}, \quad \bullet = k, \ell. \quad (65)$$

The two contributions are examined in the subsections below. There, as well as above, all quantities with subscript ℓ and p belong to surface $\partial\mathcal{B}_\ell$, while all other quantities, in particular the contact tractions, are primarily associated with surface $\partial\mathcal{B}_k$.

B.1 Normal contact

Here we consider the penalty method

$$\mathbf{t}_n = -\epsilon_n g_n \mathbf{n}_p, \quad \text{if } g_n < 0, \quad (66)$$

where

$$g_n = (\mathbf{x}_k - \mathbf{x}_p) \cdot \mathbf{n}_p, \quad (67)$$

is the normal gap at \mathbf{x}_k . This formulation falls into the contact-interaction class P according to the classification of [1]. There the tangent is derived in detail. We find

$$\begin{aligned} \frac{\partial \mathbf{t}_n}{\partial \mathbf{u}_k^e} &= -\epsilon_n \mathbf{n}_p \frac{\partial g_n}{\partial \mathbf{u}_k^e} - \epsilon_n g_n \frac{\partial \mathbf{n}_p}{\partial \mathbf{u}_k^e}, \\ \frac{\partial \mathbf{t}_n}{\partial \mathbf{u}_\ell^e} &= -\epsilon_n \mathbf{n}_p \frac{\partial g_n}{\partial \mathbf{u}_\ell^e} - \epsilon_n g_n \frac{\partial \mathbf{n}_p}{\partial \mathbf{u}_\ell^e}, \end{aligned} \quad (68)$$

with

$$\begin{aligned} \frac{\partial g_n}{\partial \mathbf{u}_k^e} &= \mathbf{n}_p^T \mathbf{N}_k, \\ \frac{\partial g_n}{\partial \mathbf{u}_\ell^e} &= -\mathbf{n}_p^T \mathbf{N}_\ell, \end{aligned} \quad (69)$$

and

$$\begin{aligned} \frac{\partial \mathbf{n}_p}{\partial \mathbf{u}_k^e} &= \frac{1}{g_n} \left[\mathbf{I} - \mathbf{n}_p \otimes \mathbf{n}_p - c_p^{\alpha\beta} \mathbf{a}_\alpha^p \otimes \mathbf{a}_\beta^p \right] \mathbf{N}_k, \\ \frac{\partial \mathbf{n}_p}{\partial \mathbf{u}_\ell^e} &= -\frac{1}{g_n} \left[\mathbf{I} - \mathbf{n}_p \otimes \mathbf{n}_p - c_p^{\alpha\beta} \mathbf{a}_\alpha^p \otimes \mathbf{a}_\beta^p \right] \mathbf{N}_\ell - c_p^{\alpha\beta} \mathbf{a}_\alpha^p \otimes \mathbf{n}_p \mathbf{N}_{\ell,\beta}, \end{aligned} \quad (70)$$

see [1], appendix C. Combing this we have

$$\begin{aligned} \frac{\partial \mathbf{t}_n}{\partial \mathbf{u}_k^e} &= \frac{\partial \mathbf{t}_n}{\partial \mathbf{x}_k} \mathbf{N}_k, \\ \frac{\partial \mathbf{t}_n}{\partial \mathbf{u}_\ell^e} &= -\frac{\partial \mathbf{t}_n}{\partial \mathbf{x}_k} \mathbf{N}_\ell + \epsilon_n g_n c_p^{\alpha\beta} \mathbf{a}_\alpha^p \otimes \mathbf{n}_p \mathbf{N}_{\ell,\beta}, \end{aligned} \quad (71)$$

with

$$\frac{\partial \mathbf{t}_n}{\partial \mathbf{x}_k} = -\epsilon_n \left[\mathbf{I} - c_p^{\alpha\beta} \mathbf{a}_\alpha^p \otimes \mathbf{a}_\beta^p \right]. \quad (72)$$

We note that if $g_n = 0$ and/or $b_{\alpha\beta}^p = 0$, we have $c_p^{\alpha\beta} = a_p^{\alpha\beta}$ so that the expression in parenthesis simplifies into

$$\mathbf{I} - a_p^{\alpha\beta} \mathbf{a}_\alpha^p \otimes \mathbf{a}_\beta^p = \mathbf{n}_p \otimes \mathbf{n}_p. \quad (73)$$

B.2 Tangential sticking step

For sticking, the tangential contact traction is given by

$$\mathbf{t}_t = \epsilon_t (\mathbf{x}_\ell(\boldsymbol{\xi}_p) - \mathbf{x}_\ell(\boldsymbol{\xi}_s^n)). \quad (74)$$

Here we have omitted the superscript $n + 1$ for convenience. All quantities without this superscript are implied to be evaluated at step $n + 1$. With $\mathbf{x}_p := \mathbf{x}_\ell(\boldsymbol{\xi}_p)$ we now find

$$\begin{aligned} \frac{\partial \mathbf{t}_t}{\partial \mathbf{u}_k^e} &= \epsilon_t \frac{\partial \mathbf{x}_p}{\partial \mathbf{u}_k^e}, \\ \frac{\partial \mathbf{t}_t}{\partial \mathbf{u}_\ell^e} &= \epsilon_t \left(\frac{\partial \mathbf{x}_p}{\partial \mathbf{u}_\ell^e} - \frac{\partial \mathbf{x}_\ell(\boldsymbol{\xi}_s^n)}{\partial \mathbf{u}_\ell^e} \right), \end{aligned} \quad (75)$$

with

$$\begin{aligned}\frac{\partial \mathbf{x}_p}{\partial \mathbf{u}_k^e} &= c_p^{\alpha\beta} \mathbf{a}_\alpha^p \otimes \mathbf{a}_\beta^p \mathbf{N}_k , \\ \frac{\partial \mathbf{x}_p}{\partial \mathbf{u}_\ell^e} &= \mathbf{N}_\ell(\boldsymbol{\xi}_p) - c_p^{\alpha\beta} \mathbf{a}_\alpha^p \otimes \left(\mathbf{a}_\beta^p \mathbf{N}_\ell(\boldsymbol{\xi}_p) - g_n \mathbf{n}_p \mathbf{N}_{\ell,\beta}(\boldsymbol{\xi}_p) \right) ,\end{aligned}\tag{76}$$

([1], appendix B) and

$$\frac{\partial \mathbf{x}_\ell(\boldsymbol{\xi}_s^n)}{\partial \mathbf{u}_\ell^e} = \mathbf{N}_\ell(\boldsymbol{\xi}_s^n) .\tag{77}$$

Combining the last equations gives

$$\begin{aligned}\frac{\partial \mathbf{t}_t}{\partial \mathbf{u}_k^e} &= \frac{\partial \mathbf{t}_t}{\partial \mathbf{x}_k} \mathbf{N}_k , \\ \frac{\partial \mathbf{t}_t}{\partial \mathbf{u}_k^e} &= -\frac{\partial \mathbf{t}_t}{\partial \mathbf{x}_k} \mathbf{N}_\ell + \epsilon_t (\mathbf{N}_\ell - \mathbf{N}_\ell(\boldsymbol{\xi}_s^n)) + \epsilon_t g_n c_p^{\alpha\beta} \mathbf{a}_\alpha^p \otimes \mathbf{n}_p \mathbf{N}_{\ell,\beta} ,\end{aligned}\tag{78}$$

with

$$\frac{\partial \mathbf{t}_t}{\partial \mathbf{x}_k} = \epsilon_t c_p^{\alpha\beta} \mathbf{a}_\alpha^p \otimes \mathbf{a}_\beta^p .\tag{79}$$

Unless otherwise specified, all \mathbf{N}_ℓ are evaluated at $\boldsymbol{\xi}_p$. If $\epsilon_t = \epsilon_n$, several terms in Eqs. (71) and (78) cancel and the resulting stiffness contribution is symmetric.

B.3 Tangential sliding step

For a sliding step the tangential contact traction is

$$\mathbf{t}_t = \mu p \mathbf{n}_t , \quad p = -\epsilon_n g_n , \quad \mathbf{n}_t = \mathbf{t}_t^{\text{trial}} / \|\mathbf{t}_t^{\text{trial}}\| ,\tag{80}$$

where we are again skipping superscript $n + 1$. The trial traction $\mathbf{t}_t^{\text{trial}}$ is defined through Eq. (74). With the help of Eq. (69) we now find

$$\begin{aligned}\frac{\partial \mathbf{t}_t}{\partial \mathbf{u}_k^e} &= -\mu \epsilon_n \mathbf{n}_t \otimes \mathbf{n}_p \mathbf{N}_k + \mu p \frac{\partial \mathbf{n}_t}{\partial \mathbf{u}_k^e} , \\ \frac{\partial \mathbf{t}_t}{\partial \mathbf{u}_\ell^e} &= \mu \epsilon_n \mathbf{n}_t \otimes \mathbf{n}_p \mathbf{N}_\ell(\boldsymbol{\xi}_p) + \mu p \frac{\partial \mathbf{n}_t}{\partial \mathbf{u}_\ell^e} ,\end{aligned}\tag{81}$$

with

$$\begin{aligned}\frac{\partial \mathbf{n}_t}{\partial \mathbf{u}_k^e} &= \frac{1}{\|\mathbf{t}_t^{\text{trial}}\|} \left[\mathbf{I} - \mathbf{n}_t \otimes \mathbf{n}_t \right] \frac{\partial \mathbf{t}_t^{\text{trial}}}{\partial \mathbf{u}_k^e} , \\ \frac{\partial \mathbf{n}_t}{\partial \mathbf{u}_\ell^e} &= \frac{1}{\|\mathbf{t}_t^{\text{trial}}\|} \left[\mathbf{I} - \mathbf{n}_t \otimes \mathbf{n}_t \right] \frac{\partial \mathbf{t}_t^{\text{trial}}}{\partial \mathbf{u}_\ell^e} ,\end{aligned}\tag{82}$$

where the last pieces are given in Sec. B.2 above. Combining everything gives

$$\begin{aligned}\frac{\partial \mathbf{t}_t}{\partial \mathbf{u}_k^e} &= \frac{\partial \mathbf{t}_t}{\partial \mathbf{x}_k} \mathbf{N}_k , \\ \frac{\partial \mathbf{t}_t}{\partial \mathbf{u}_k^e} &= -\frac{\partial \mathbf{t}_t}{\partial \mathbf{x}_k} \mathbf{N}_\ell + \epsilon_t \mathbf{P} (\mathbf{N}_\ell - \mathbf{N}_\ell(\boldsymbol{\xi}_s^n)) + \epsilon_t g_n c_p^{\alpha\beta} \mathbf{P} \mathbf{a}_\alpha^p \otimes \mathbf{n}_p \mathbf{N}_{\ell,\beta} ,\end{aligned}\tag{83}$$

with

$$\frac{\partial \mathbf{t}_t}{\partial \mathbf{x}_k} = -\mu \epsilon_n \mathbf{n}_t \otimes \mathbf{n}_p + \epsilon_t c_p^{\alpha\beta} \mathbf{P} \mathbf{a}_\alpha^p \otimes \mathbf{a}_\beta^p ,\tag{84}$$

and

$$\mathbf{P} := \frac{\mu p}{\|\mathbf{t}_t^{\text{trial}}\|} \left[\mathbf{I} - \mathbf{n}_t \otimes \mathbf{n}_t \right] .\tag{85}$$

References

- [1] Sauer RA, De Lorenzis L. A computational contact formulation based on surface potentials. *Comput. Methods Appl. Mech. Engrg.* 2013; **253**:369–395.
- [2] Papadopoulos P, Jones RE, Solberg JM. A novel finite element formulation for frictionless contact problems. *Int. J. Numer. Meth. Engrg.* 1995; **38**:2603–2617.
- [3] Laursen TA, Simo JC. A continuum-based finite element formulation for the implicit solution of multibody, large deformation frictional contact problems. *Int. J. Numer. Meth. Engrg.* 1993; **36**:3451–3485.
- [4] Fischer KA, Wriggers P. Mortar based frictional contact formulation for higher order interpolations using the moving friction cone. *Comput. Methods Appl. Mech. Engrg.* 2006; **195**:5020–5036.
- [5] Papadopoulos P, Solberg JM. A Lagrange multiplier method for the finite element solution of frictionless contact problems. *Math. Comp. Model.* 1998; **28**:373–384.
- [6] Jones RE, Papadopoulos P. A novel three-dimensional contact finite element based on smooth pressure interpolations. *Int. J. Numer. Meth. Engrg.* 2001; **51**:791–811.
- [7] Jones RE, Papadopoulos P. A yield-limited Lagrange multiplier formulation for frictional contact. *Int. J. Numer. Meth. Engrg.* 2000; **48**:1127–1149.
- [8] Jones RE, Papadopoulos P. Simulating anisotropic frictional response using smoothly interpolated traction fields. *Comput. Methods Appl. Mech. Engrg.* 2006; **195**:588–613.
- [9] Laursen TA. *Computational Contact and Impact Mechanics: Fundamentals of modeling interfacial phenomena in nonlinear finite element analysis*. Springer, 2002.
- [10] Wriggers P. *Computational Contact Mechanics*. 2nd edn., Springer, 2006.
- [11] Lu J. Isogeometric contact analysis: Geometric basis and formulation for frictionless contact. *Comput. Methods Appl. Mech. Engrg.* 2011; **200**(5-8):726–741.
- [12] Sauer RA. Enriched contact finite elements for stable peeling computations. *Int. J. Numer. Meth. Engrg.* 2011; **87**:593–616.
- [13] Temizer I, Wriggers P, Hughes TJR. Contact treatment in isogeometric analysis with NURBS. *Comput. Methods Appl. Mech. Engrg.* 2011; **200**:1100–1112.
- [14] De Lorenzis L, Wriggers P, Zavarise G. A mortar formulation for 3D large deformation contact using NURBS-based isogeometric analysis and the augmented Lagrangian method. *Comp. Mech.* 2012; **49**:1–20.
- [15] De Lorenzis L, Temizer I, Wriggers P, Zavarise G. A large deformation frictional contact formulation using NURBS-based isogeometric analysis. *Int. J. Numer. Meth. Engrg.* 2011; **87**:1278–1300.
- [16] Temizer I, Wriggers P, Hughes TJR. Three-dimensional mortar-based frictional contact treatment in isogeometric analysis with NURBS. *Comput. Methods Appl. Mech. Engrg.* 2012; **209-212**:115–128.
- [17] Sauer RA. Local finite element enrichment strategies for 2D contact computations and a corresponding postprocessing scheme. *Comput. Mech.* 2013; **52**(2):301–319.

- [18] Padmanabhan V, Laursen TA. A framework for development of surface smoothing procedures in large deformation frictional contact analysis. *Finite Elem. Anal. Des.* 2001; **37**:173–198.
- [19] Krstulovic-Opara L, Wriggers P, Korelc J. A C^1 -continuous formulation for 3D finite deformation friction contact. *Comp. Mech.* 2002; **29**:27–42.
- [20] Stadler M, Holzzapfel GA. Subdivision schemes for smooth contact surfaces of arbitrary mesh topology in 3D. *Int. J. Numer. Meth. Engng.* 2004; **60**:1161–1195.
- [21] Simo JC, Hughes TJR. *Computational Inelasticity*. Springer, 1998.
- [22] Konyukhov A, Schweizerhof K. Covariant description for frictional contact problems. *Comput. Mech.* 2005; **35**:190–213.
- [23] Lengiewicz J, Korelc J, Stupkiewicz S. Automation of finite element formulations for large deformation contact problems. *Int. J. Numer. Meth. Engng.* 2010; **85**:1252–1279.
- [24] Agelet de Saracibar C. A new frictional time integration algorithm for large slip multi-body frictional contact problems. *Comp. Meth. Appl. Mech. Engrg.* 1997; **142**:303–334.
- [25] Corbett CJ, Sauer RA. NURBS-enriched contact finite elements. *Comput. Methods Appl. Mech. Engrg.* 2014; **275**:55–75.
- [26] Puso MA, Laursen TA. A mortar segment-to-segment frictional contact method for large deformations. *Comput. Methods Appl. Mech. Engrg.* 2004; **193**:4891–4913.
- [27] Kikuchi N, Oden J. *Contact Problems in Elasticity: A Study of Variational Inequalities and Finite Element Methods*. SIAM, 1988.
- [28] Solberg JM, Jones RE, Papadopoulos P. A family of simple two-pass dual formulations for the finite element solution of contact problems. *Comput. Methods Appl. Mech. Engrg.* 2007; **196**:782–802.
- [29] Zienkiewicz OC, Taylor RL. *The Finite Element Method for Solid and Structural Mechanics*. 6th edn., Butterworth-Heinemann, 2005.
- [30] Johnson KL. *Contact Mechanics*. Cambridge University Press, 1985.
- [31] Arnold DN, Brezzi F, Cockburn B, Marini LD. Unified analysis of discontinuous Galerkin methods for elliptic problems. *SIAM J. Numer. Anal.* 2002; **39**(5):1749–1779.
- [32] Sauer RA, Duong TX, Corbett CJ. A computational formulation for constrained solid and liquid membranes considering isogeometric finite elements. *Comput. Methods Appl. Mech. Engrg.* 2014; **271**:48–68.